



HAL
open science

On Earth's habitability over the Sun's main-sequence history: joint influence of space weather and Earth's magnetic field evolution

J. Varela, A. S. Brun, A. Strugarek, V. Réville, P. Zarka, F. Pantellini

► To cite this version:

J. Varela, A. S. Brun, A. Strugarek, V. Réville, P. Zarka, et al.. On Earth's habitability over the Sun's main-sequence history: joint influence of space weather and Earth's magnetic field evolution. *Monthly Notices of the Royal Astronomical Society*, 2023, 525, pp.4008-4025. 10.1093/mnras/stad2519 . insu-04473133

HAL Id: insu-04473133

<https://insu.hal.science/insu-04473133>

Submitted on 23 Feb 2024

HAL is a multi-disciplinary open access archive for the deposit and dissemination of scientific research documents, whether they are published or not. The documents may come from teaching and research institutions in France or abroad, or from public or private research centers.

L'archive ouverte pluridisciplinaire **HAL**, est destinée au dépôt et à la diffusion de documents scientifiques de niveau recherche, publiés ou non, émanant des établissements d'enseignement et de recherche français ou étrangers, des laboratoires publics ou privés.

On Earth's habitability over the Sun's main-sequence history: joint influence of space weather and Earth's magnetic field evolution

J. Varela ¹★, A. S. Brun,² A. Strugarek ², V. Réville,³ P. Zarka⁴ and F. Pantellini⁵

¹Physics Department, Universidad Carlos III de Madrid, E-28911 Leganes, Spain

²Laboratoire AIM, CEA/DRF – CNRS – Univ. Paris Diderot – IRFU/DAP, Paris-Saclay, F-91191 Gif-sur-Yvette Cedex, France

³IRAP, Université Toulouse III-Paul Sabatier, CNRS, CNES, F-31062 Toulouse, France

⁴LESIA & USN, Observatoire de Paris, CNRS, PSL/SU/UPMC/UPD/UO, Place J. Janssen, F-92195 Meudon, France

⁵LESIA, Observatoire de Paris, Université PSL, CNRS, Sorbonne Université, Université de Paris, 5 place Jules Janssen, F-92195 Meudon, France

Accepted 2023 August 17. Received 2023 August 17; in original form 2023 May 2

ABSTRACT

The aim of this study is to analyse the Earth habitability with respect to the direct exposition of the Earth atmosphere to the solar wind (SW) along the Sun's evolution on the main sequence including the realistic evolution of the space weather conditions and the Earth magnetic field. The MHD code PLUTO in spherical coordinates is applied to perform parametric studies with respect to the SW dynamic pressure and the interplanetary magnetic field intensity for different Earth magnetic field configurations. Quiet space weather conditions may not impact the Earth habitability. On the other hand, the impact of interplanetary coronal mass ejections (ICME) could lead to the erosion of the primary Earth atmosphere during the Hadean eon. A dipolar field of 30 μT is strong enough to shield the Earth from the Eo-Archean age as well as 15 and 5 μT dipolar fields from the Meso-Archean and Meso-Proterozoic, respectively. Multipolar weak field period during the Meso-Proterozoic age may not be a threat for ICME-like space weather conditions if the field intensity is at least 15 μT and the ratio between the quadrupolar (Q) and dipolar (D) coefficients is $\frac{Q}{D} \leq 0.5$. By contrast, the Earth habitability in the Phanerozoic eon (including the present time) can be hampered during multipolar low field periods with a strength of 5 μT and $\frac{Q}{D} \geq 0.5$ associated with geomagnetic reversals. Consequently, the effect of the SW should be considered as a possible driver of Earth's habitability.

Key words: MHD – Earth – planets and satellites: magnetic fields – planet–star interactions.

1 INTRODUCTION

The analysis of the space weather in the last decades has demonstrated the essential role of the solar wind (SW) and interplanetary magnetic field (IMF) on the Earth magnetosphere, ionosphere, thermosphere, and exosphere state (Poppe & Jorden 2006; González Hernández et al. 2014). That means, space weather conditions can introduce constraints on the habitability of the Earth and exoplanets with respect to the shielding provided by planetary magnetospheres, avoiding the sterilizing effect of the stellar wind on the surface (Strugarek et al. 2015; Garraffo, Drake & Cohen 2016; Gallet et al. 2017; Linsky 2019; Airapetian et al. 2020; Varela et al. 2022b). Recent studies also indicate the SW may cause the depletion of the Earth atmosphere, particularly volatile molecules such as water by thermal and non-thermal escape (Lundin, Lammer & Ribas 2007; Moore & Khazanov 2010; Jakosky et al. 2015) as well as lead to damages on biological structures (Sihver & Mortazavi 2021; Zenchenko & Breus 2021).

The largest perturbations of the Earth magnetosphere are observed during periods of extreme space weather conditions associated with coronal mass ejections (CME; Cane, Richardson & St. Cyr 2000; Richardson, Cliver & Cane 2001; Wang et al. 2003; Lugaz et al.

2015; Wu & Lepping 2015). The CMEs are solar eruptions caused by magnetic reconnections in the star corona (Low 2001; Howard 2006), leading to the generation of streams of charged particles and a magnetic cloud that propagates in the interplanetary medium (ICME; Sheeley et al. 1985; Gosling 1990; Neugebauer & Goldstein 1997; Cane & Richardson 2003). During the impact of an ICME with the Earth, the SW dynamic pressure and the intensity of the IMF can increase by two orders of magnitude (Gosling et al. 1991; Huttunen et al. 2002; Manchester et al. 2004; Schwenn et al. 2005; Riley 2012; Howard 2014; Mays et al. 2015; Kay et al. 2017; Savani et al. 2017; Salman et al. 2018; Hapgood 2019; Kilpua et al. 2019; Regnault et al. 2020, 2022). Damages in spacecrafts (Choi et al. 2011; Molera Calvés et al. 2014; Nwankwo, Chakrabarti & Weigel 2015) and critical infrastructures such as electric power grids (Cannon et al. 2013) are observed during ICME. In addition, ICMEs may hamper the habitability of exoplanets hosted by stars showing a large magnetic activity (larger ICME recurrence and intensity than the Sun; Schaefer, King & Deliyannis 2000; Khodachenko et al. 2007; Lammer et al. 2007; Balona 2012).

Early stages of the Sun evolution showed a fast rotation rate and high magnetic activity (Pizzolato et al. 2003; Emeriau-Viard & Brun 2017) that decreased along the Sun's evolution on the main sequence (Fabbian et al. 2017; Folsom et al. 2017), a mechanism known as gyro-chronology (Skumanich 1972; Barnes 2003). Accordingly, the forcing of the SW and IMF on the Earth magnetosphere, that is to

* E-mail: deviriam@hotmail.com, deviriam@gmail.com

say the space weather conditions, also changed (Réville et al. 2016; Carolan et al. 2019; Ahuir, Brun & Strugarek 2020; Varela et al. 2022b). The SW dynamic pressure and IMF intensity were much higher at early stages of the Sun main sequence compared to the present days (Airapetian 2016; Lugaz 2019), thus the perturbations induced by the young Sun on the Earth magnetosphere were stronger (Stereberg et al. 2011; Carolan et al. 2019; Varela et al. 2022b), and the Earth likely exposed to more powerful and recurrent ICMs (Stereberg et al. 2011; Shibayama et al. 2013; Airapetian, Gloer & Danchi 2014; Airapetian, Gloer & Guillaume 2015) leading to an increase of the ion transport in the inner magnetosphere (Zhang et al. 2022).

Geological surveys (Schwarz & Symons 1969; McElhinny & McFadden 1998; Tarduno et al. 2007, 2010, 2020; Tarduno, Blackman & Mamajek 2014) and geodynamo numerical models (Aubert, Labrosse & Poitou 2009; Aubert, Tarduno & Johnson 2010; Driscoll 2016; Davies et al. 2021; Aubert et al. 2022) indicate a large variability of the Earth magnetic field intensity and topology along the Sunders evolution on the main sequence. There are evidences of weak field periods during the Paleo-Archean and Meso-Archean eras as well as the Proterozoic eon showing dipolar field intensities below 20 μT (Morimoto et al. 1997; Elming et al. 2009; Di Chiara et al. 2017). In addition, weak field periods are also identified along the Paleozoic (Cambrian, Devonian, and Carboniferous periods; Hawkins et al. 2019a, 2021; Thallner et al. 2021) and Mesozoic eras (Triassic, Jurassic, and Paleogene periods; Prevot et al. 1990; Kostrov et al. 1997; Juarez et al. 1998; Heunemann et al. 2004; Calvo-Rathert et al. 2021). On the other hand, strong dipolar field periods could exist during the Hadean eon and Eo-Archean era showing intensities above 40 μT (Hale & Dunlop 1984; Tarduno et al. 2020). Nevertheless, periods of dipolar field with intensities comparable to the present time were also held in the Meso-Proterozoic and Neo-Archean eras as well as in the Cretaceous and Neogene periods (Yoshihara & Hamano 2000; Di Chiara et al. 2021; Kaya et al. 2023). In addition, there are evidences of multipolar low field configurations during the Proterozoic age, the Devonian and Cretaceous periods linked to geomagnetic reversals (Bogue & Merrill 1992; McElhinny & McFadden 1998; Gubbins 2008), characterized by large quadrupolar components of the magnetic field similar to the present Hermean magnetic field (Guyodo & Valet 1999; Lhuillier et al. 2016; Shcherbakova et al. 2017).

The aim of the present study is to analyse the Earth habitability along the Sun's evolution on the main sequence from the point of view of the space weather conditions and Earth magnetic field configuration, that is to say, identifying if the Earth magnetosphere was able to protect the planet from the direct impact of the SW in the last 4600 million years. In addition, the study explores the minimum requirements of the magnetic field in the next 3000 million years to protect the Earth (Posterum eons). The study methodology is based on the extensive use of parametric analysis using a global MHD model, calculating the magnetosphere deformation for different space weather conditions and configurations of the Earth magnetic field. The study includes space weather conditions from quiet to super ICME events as well as dipolar and multipolar fields with intensities consistent with the paleomagnetism data.

The analysis of the Earth habitability conditions is performed with respect to the magnetopause standoff distance, assuming that the Earth habitability could be hampered if the magnetopause collapses on to the Earth surface, that is to say, the SW precipitates directly towards the Earth. Consequently, the magnetosphere fails to protect both the Earth surface and atmosphere. It should be noted that there are other important factors that constrain the Earth habitability, for

example the EUV, X-ray, and cosmic rays (Buccino, Lemarchand & Mauas 2007; Sanz-Forcada et al. 2010; Airapetian et al. 2017; Rodgers-Lee et al. 2021; Johnstone, Bartel & Gudel 2021b). In particular, large EUV and X-ray fluxes during the Hadean and Archean eons may have caused an expansion of the ionosphere affecting the standoff distance of the bow shock and magnetopause (Ribas et al. 2005; Tu et al. 2015; Lammer et al. 2018). Nevertheless, the SW precipitation should be understood as one of the main concerns for the Earth habitability along the Sun's evolution on the main sequence (Zendejas, Segura & Raga 2010; See et al. 2014; Blackman & Tarduno 2018; Rodriguez-Mozos & Moya 2019; Chebly, Alvarado-Gómez & Poppenhaeger 2022).

MHD models are routinely used to analyse the interaction of the SW and IMF with planetary magnetospheres (Kabin et al. 2008; Strugarek et al. 2014, 2015; Jia et al. 2015; Varela, Pantellini & Moncuquet 2015; Paul, Vaidya & Strugarek 2022). Previous studies indicate a stronger compression of the bow shock as the dynamic pressure of the SW increases and a modification of the planetary magnetosphere topology caused by the interaction between the IMF and the planetary magnetic field (Slavin & Holzer 1979; Kabin et al. 2000; Slavin et al. 2009; Varela, Pantellini & Moncuquet 2016d). MHD models are also applied to study the effect of the space weather on the Earth magnetosphere's large-scale structures, for example the Bow Shock (Samsonov, Sibeck & Imber 2007; Andréevová et al. 2008; Němeček et al. 2011; Mejnertsen et al. 2018), the Magnetosheath (Ogino, Walker & Ashour-Abdalla 1992; Wang, Raeder & Russell 2004), the magnetopause stand off distance (Cairns & Lyon 1995, 1996; Wang et al. 2012) and the magnetotail (Laitinen et al. 2005; Wang et al. 2014). In particular, global MHD models reproduce the strong deformations induced by ICMs in the Earth magnetosphere (Wu & Lepping 2002; Wu, Lepping & Gopalswamy 2006; Shen et al. 2011; Ngwira et al. 2013; Wu et al. 2016; Scolini et al. 2018; Torok et al. 2018) leading to an important decrease of the magnetopause stand off distance (Sibeck, Lopez & Roelof 1991; Dušák et al. 2010; Liu et al. 2015; Němeček et al. 2016; Grygorov et al. 2017; Samsonov et al. 2020). It should be noted that MHD codes were validated comparing the simulation results with ground-based magnetometers and spacecraft measurements (Raeder et al. 2001; Wang et al. 2003; Den et al. 2006; Honkonen et al. 2013; Facskó et al. 2016). Nevertheless, kinetic effects are also important but are out of the scope of the present study and may have effects on the final conclusions (Xu et al. 2015; Omelchenko et al. 2021; Lembege, Cai & Ekawati 2022).

The analysis is performed using the single fluid MHD code PLUTO in spherical 3D coordinates (Mignone et al. 2007). The numerical framework was already applied to model global structures of the Hermean magnetosphere (Varela et al. 2015, 2016a, b, d), the effect of ICME-like space weather conditions on the Earth magnetosphere (Varela et al. 2022b), slow modes in the Hermean magnetosphere (Varela, Pantellini & Moncuquet 2016c) as well as the radio emission from the Hermean and exoplanetary magnetospheres (Varela et al. 2016e, 2018, 2022a).

This paper is structured as follows. There is a basic description of the simulation model in Section 2. The space weather models used in the analysis are discussed in Section 3. The Earth habitability from the Hadean eon to the present era with respect to the intensity of a dipolar magnetic field is analysed in Section 4. The consequences on the Earth habitability of periods with multipolar magnetic fields are studied in Section 5. The minimum Earth habitability requirements for a decaying Earth magnetic field in future eons is analysed in Section 6. The effect of an expanded ionosphere due to large EUV and X-ray fluxes on the Earth habitability is introduced in Section 7.

		Geological time Beginning-End (Mya)	Paleomagnetic data		Earth B field model		
			Dipole (μT)	Multipolar	Dipole (μT)	Multipolar (μT , Q/D)	
Hadean		4,567 - 4,000	> 45		45		
Archean	EoArchean	4,000 - 3,640	> 40		45		
	PaleoArchean	3,600 - 3,200	< 25		15		
	MesoArchean	3,200 - 2,800	< 25		15		
	NeoArchean	2,800 - 2,500	\approx 30		30		
Proterozoic	Paleoproterozoic	2,500 - 1,600	< 25	YES	15	15, 0.2 and 0.5	
	MesoProterozoic	1,600 - 1,000	\approx 30	YES	30	15, 0.2 and 0.5	
	NeoProterozoic	Tonian	1,000 - 720	< 25	YES	15	15, 0.2 and 0.5
		Cryogenian	720 - 635	< 25	YES	15	15, 0.2 and 0.5
		Ediacaran	635 - 538.8	< 25	YES	15	15, 0.2 and 0.5
Phanerozoic	Paleozoic	Cambrian	538.8 - 485.4	< 10		5	
		Ordovician	485.4 - 443.8				
		Silurian	443.8 - 419.2				
		Devonian	419.2 - 358.9	< 10	YES	5	5, 0.2 and 0.5
		Carboniferous	358.9 - 298.9	< 10		5	
		Permian	298.9 - 251.9				
	Mesozoic	Triassic	251.9 - 201.4	< 10		5	
		Jurassic	201.4 - 145	< 25		15	
		Cretaceous	145 - 66		YES		15, 0.2 and 0.5
	Cenozoic	Paleogene	66 - 23	< 25		15	
		Neogene	23 - 2.6	\approx 30		30	
		Quaternary	2.6 - 0	\approx 30		30	

Figure 1. Earth magnetic field intensity (first column) and evidence of large multipolar components (second column) obtained from Paleomagnetic data. Earth magnetic field model applied to study geological times with a dominant dipolar component (third column) or multipolar configurations (fourth column).

Finally, Section 8 shows the summary of the study main conclusions discussed in the context of other authors results.

2 NUMERICAL MODEL

The analysis is performed using the ideal MHD version of the open-source code PLUTO in spherical coordinates. The model calculates the evolution of a single-fluid ideal plasma in the non-resistive and inviscid limit (Mignone et al. 2007). A detailed description of the model equations, boundary conditions, and upper ionosphere model can be found in Varela et al. (2022b).

The simulations are performed using a grid of 128 radial points, 48 bins in the polar angle θ and 96 in the azimuthal angle ϕ , equidistant in the radial direction. The simulation domain is confined between two concentric shells around the Earth, an outer boundary (R_{out}) fixed at $30 R_E$ (R_E is the Earth radius) and an inner boundary (R_{in}) whose radial location depends on the intensity of the Earth magnetic field. In addition, below the inner boundary of the simulation domain, an upper ionosphere coupling region is added based on the electric field generated by the field-aligned currents providing the plasma velocity at the upper ionosphere (Büchner, Dum & Scholer 2003). The radial extension of the upper ionosphere coupling region (ΔR_{ion}) is fixed to $0.2 R_E$. The effect of the ionosphere expansion caused by large EUV and X-ray fluxes in the Hadean and Archean eons (Ribas et al. 2005; Tu et al. 2015; Lammer et al. 2018) is introduced in the model. This first attempt to improve the ionosphere model is discussed in the Appendix section. Such extended model is not used in all the simulation set, only in the cases studied in Section 7.

A set of Earth's magnetic field configurations is considered in the analysis. Low to high dipolar magnetic field periods are analysed using dipole models with an intensity of 5, 15, 30, and 45 μT . The intensity of the magnetic field models is defined at the surface of the Earth in the equatorial region [ranging for the case of the present Earth between 25 and 65 μT between the equator and the poles (Finlay et al. 2010)]. Multipolar low field periods are explored by models including dipolar and quadrupolar field components, parametrized by the ratio between the quadrupole (Q) and dipole (D) coefficients, Q/D , and the field intensity. Particularly, the simulations are performed for the models with $Q/D = 0.2$ and 0.5 as well as field intensity of 5 and 15 μT (the combination of dipolar and quadrupolar components of the magnetic field leads to the given intensity at the Earth surface in the equatorial region). Future scenarios are simulated as a decaying dipolar field with an intensity of 0.1 and 1 μT (geo-dynamo extinction). Fig. 1 summarizes the Paleomagnetic data obtained from geological surveys and the Earth magnetic field model applied to study different geological times.

The Earth magnetic field is rotated 90° in the YZ plane with respect to the grid poles, a transformation required to avoid spurious plasma outflows in the cusp regions linked to an issue with the boundary condition where geometrical and magnetical poles overlap (no special treatment was included for the singularity at the magnetic poles). Consequently, the IMF orientation is adapted accordingly. The tilt of the Earth rotation axis is included (fixed at 23° with respect to the ecliptic plane). The effect of the Earth rotation is not included in the analysis for simplicity.

Table 1. Main simulation parameters for each Earth magnetic field model: quadrupole–dipole coefficients ratio, field intensity (at the equatorial region of the Earth surface), inner boundary location, SW dynamic pressure range, IMF intensity range, and Earth magnetic field configuration.

Topology (Q/D)	B_E (μT)	R_{in} (R_E)	P_d (nPA)	B_{IMF} (nT)	Configuration
0	0.1	1.0	1–5	1–50	Decayed dipole
0	1	1.0	1–100	1–150	Decayed dipole
0	5	1.5	1–200	1–200	Low dipole field
0	15	2.25	1–200	1–200	Low dipole field
0	30	2.5	1–200	1–200	Standard dipole field
0	45	2.5	1–250	1–250	High dipole field
0.2	5	1.2	1–150	1–200	Multipolar
0.5	5	1.2	1–50	1–150	Multipolar
0.2	15	1.2	1–200	1–200	Multipolar
0.5	15	1.2	1–200	1–200	Multipolar

The simulation frame assumed is: z -axis is provided by the planetary magnetic axis pointing to the magnetic north pole, star–planet line is located in the XZ plane with $x_{star} > 0$ (solar magnetic coordinates) and the y -axis completes the right-handed system.

The set of simulations performed for different space weather conditions are parametrized with respect to the SW dynamic pressure and IMF intensity. A Southward IMF is assumed because it is the orientation leading to the strongest reconnection between the IMF and Earth magnetic field and the lowest magnetopause standoff distance. Consequently, the analysis provides the upper limit of the SW restrictions on the Earth habitability for a given space weather configuration. The decayed dipole simulations also include in the analysis the Northward, radial (Earth–Sun), and ecliptic (counter-clock wise) IMF orientations. It should be noted that the space weather conditions leading to a magnetopause standoff distance below the inner boundary of the simulation domain (the top of the upper ionosphere model, not the planet surface) or numerical instabilities causing the termination of the simulation are removed from the analysis.

Table 1 shows the main parameters for each Earth magnetic field model as well as the range of SW dynamic pressure and IMF intensity values explored. SW temperature is $T = 2 \times 10^5$ K in all the configurations analysed.

Fig. 2 shows a 3D view of a simulation domain for typical space weather conditions during the Cambrian period (SW dynamic pressure of 1 nPa and a Southward IMF intensity of 10 nT) for a dipolar weak field period of 5 μT . The equatorial and polar cuts indicate the SW density distribution showing the formation of the bow shock in the Earth day side due to the accumulation of plasma coming from the slowed down and diverted SW by the Earth magnetosphere. The SW flow causes the bending of the Earth magnetic field lines and the compression of the magnetosphere. The Southward IMF reconnects with the Earth magnetic field and causes the erosion of the magnetosphere in the equatorial region, reducing the efficiency of the magnetic shield to protect the Earth surface and atmosphere. The magnetopause is located several Earth radii above the surface, thus the Earth magnetic field is strong enough to avoid the direct precipitation of the SW. It should be noted that the star is not included inside the computational domain and the space weather conditions are introduced as the outer boundary conditions of the model in the day side.

The theoretical approximation of the magnetopause standoff distance is calculated as the balance between the dynamic pressure of the SW ($P_d = m_p n_{sw} v_{sw}^2/2$), the thermal pressure of the SW

($P_{th,sw} = m_p n_{sw} v_{th,sw}^2/2 = m_p n_{sw} c_{sw}^2/\gamma$), and the magnetic pressure of the IMF ($P_{mag,IMF} = B_{IMF}^2/2\mu_0$) with respect to the magnetic pressure of the compressed Earth dipolar magnetic field ($P_{mag,E} = \alpha\mu_0 M_E^2/8\pi^2 r^6$) and the thermal pressure of the magnetosphere ($P_{th,MSP} = m_p n_{MSP} v_{th,MSP}^2/2$). Here, m_p is the proton mass, n_{sw} the SW density, v_{sw} the SW velocity, c_{sw} the SW sound speed, γ the polytropic index, B_{IMF} the IMF intensity, μ_0 the vacuum magnetic permeability, α the dipole compression coefficient [$\alpha \approx 2$ (Gombosi 1994)], M_E the Earth's dipole magnetic field moment, n_{MSP} the magnetospheric plasma density and $v_{th,MSP}$ the thermal velocity of the magnetospheric plasma. This results in the expression:

$$P_d + P_{mag,sw} + P_{th,sw} = P_{mag,E} + P_{th,MSP}, \quad (1)$$

thus,

$$\frac{R_{mp}}{R_E} = \left[\frac{\alpha\mu_0 M_E^2}{4\pi^2 \left(m_p n_{sw} v_{sw}^2 + \frac{B_{IMF}^2}{\mu_0} + \frac{2m_p n_{sw} c_{sw}^2}{\gamma} - m_p n_{MSP} v_{th,MSP}^2 \right)} \right]^{(1/6)}, \quad (2)$$

with $r_{mp} = R_{mp}/R_E$ the magnetopause standoff distance. It should be noted that this expression holds for a dipolar magnetic field, not for a multipolar magnetic field. The description of a multipolar field requires introducing the effect of high order moments of the multipolar expansion in the definition of the magnetic pressure of the Earth magnetic field. The magnetopause standoff distance in the simulations analysis is defined as the last close magnetic field line on the exoplanet dayside at 0° longitude in the ecliptic plane. The data set of magnetopause standoff distance values calculated for different space weather conditions are fitted with respect to P_d and $|B|_{IMF}$ using the surface function $\log(r_{mp}) = \log(Z) + M\log(|B|_{IMF}) + N\log(P_d)$, derived from the expression $r_{mp} = Z|B|_{IMF}^M P_d^N$ with Z a proportionality constant. The critical $|B|_{IMF}$ and P_d values indicating the Earth habitability threshold are calculated as the isoline that verifies $r_{mp} = 1$, that is to say, direct precipitation of the SW towards the planet.

3 SPACE WEATHER MODELLING

The evolution of the space weather conditions generated by the Sun along the main sequence can be predicted applying different model. For example, the evolution of the SW velocity and density at the Earth orbit can be estimated using the model by Griebmeier, Zarka & Spreew (2007), which combines the empirical estimation of the evolution of the stellar mass-loss rate as a function of stellar age by Wood et al. (2005) and a model of the age-dependence of the stellar wind velocity by Newkirk (1980):

$$v_{sw}(t) = v_0 \left(1 + \frac{t}{\tau} \right)^{-0.43}, \quad (3)$$

$$n_{sw}(t) = n_0 \left(1 + \frac{t}{\tau} \right)^{-1.84 \pm 0.6}, \quad (4)$$

providing a first order of magnitude approximation of the P_d values along the Sun's evolution on the main sequence for quiet space weather conditions. ICME-like space weather conditions are defined assuming an increase of P_d by two orders of magnitude compared to the quiet conditions, consistent with the upper bound of P_d during the observed ICMEs (Gosling et al. 1991; Riley 2012; Savani et al. 2017; Salman et al. 2018; Hapgood 2019; Kilpua et al. 2019). It should be noted that super-flares may cause P_d above the parametric range analysed (Maehara et al. 2012, 2015), thus super-flares are out of the scope of the study. Next, the critical B_{IMF} required for the direct

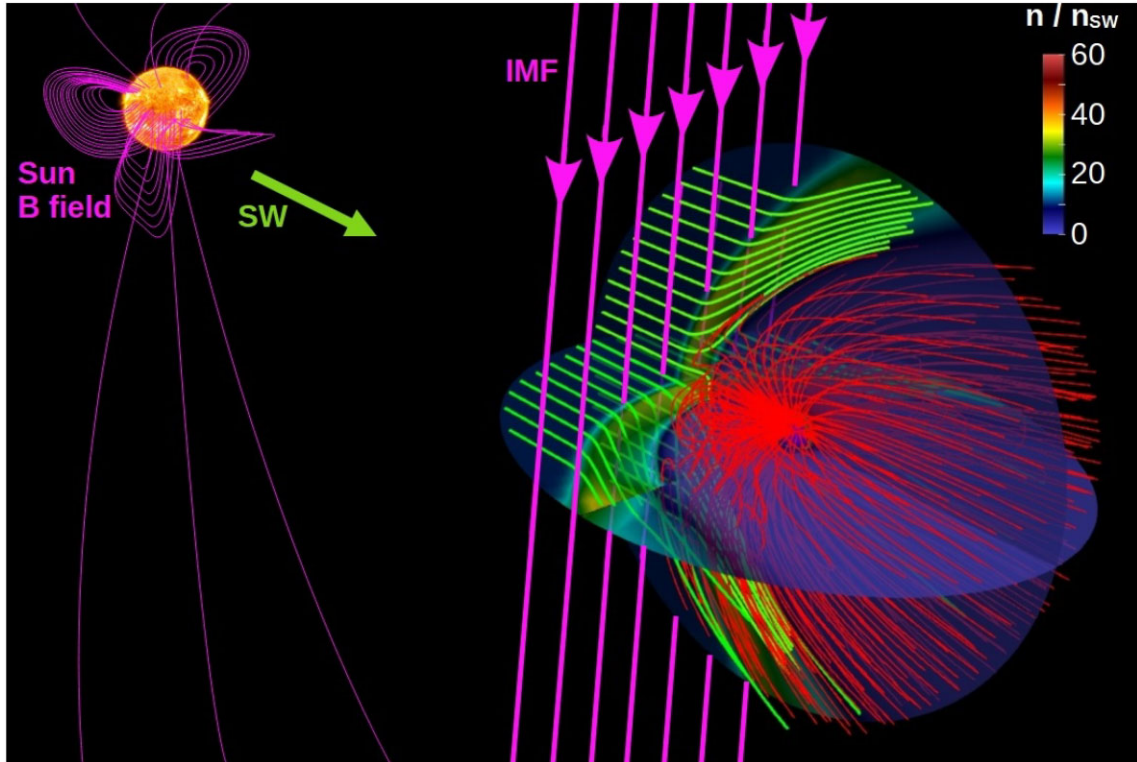


Figure 2. 3D view of a typical simulation setup. SW density distribution (colour scale), Earth magnetic field lines (red lines), and Sun magnetic field (pink lines). The bold pink arrows indicate the orientation of the IMF (Southward orientation). The green lines indicate the SW velocity stream lines.

SW deposition during quiet and ICME-like space weather conditions is calculated taking the P_d values from Grießmeier et al. (2007) and using the regression results imposing the condition $r_{mp} = 1$.

The critical B_{IMF} calculated can be compared with models that predict the IMF intensity at the Earth orbit along the Sun’s evolution on the main sequence. One possibility is using the model developed by Vidotto et al. (2014) and Carolan et al. (2019) that show a reasonable agreement with the SW dynamic pressure values suggested by Grießmeier et al. (2007). The Vidotto et al. (2014) and Carolan et al. (2019) approximation is based on a 1.50 Weber–Davis model (Weber & Davis 1967) solved using the Versatile Advection Code (VAC; Toth 1996; Johnstone et al. 2015) assuming a polytropic wind of 1.05 leading to an almost isothermal stellar wind temperature profile. If the calculated critical B_{IMF} is above the IMF intensity in Vidotto et al. (2014) and Carolan et al. (2019) model for a given geological time and dipole intensity, the Earth habitability could be jeopardized by the effect of the space weather conditions. The analysis assumes the upper bound of the IMF intensity during ICMEs is 50 times larger compared to the quiet space weather conditions provided by Vidotto et al. (2014) and Carolan et al. (2019). In the following, the combination of Grießmeier et al. (2007) and Vidotto et al. (2014); Carolan et al. (2019) models to calculate the space weather conditions is called G-V-C model.

In addition to the space weather predictions by the G-V-C model, the analysis also includes the estimations provided by the Ahuir model (Ahuir et al. 2020). Applying two different models is required to validate the analysis results, that is to say, if similar consequences on the Earth habitability are obtained using both models the study conclusions may be considered robust. Ahuir model brings power laws that describe the mass-loss, magnetic field as well as the coronal

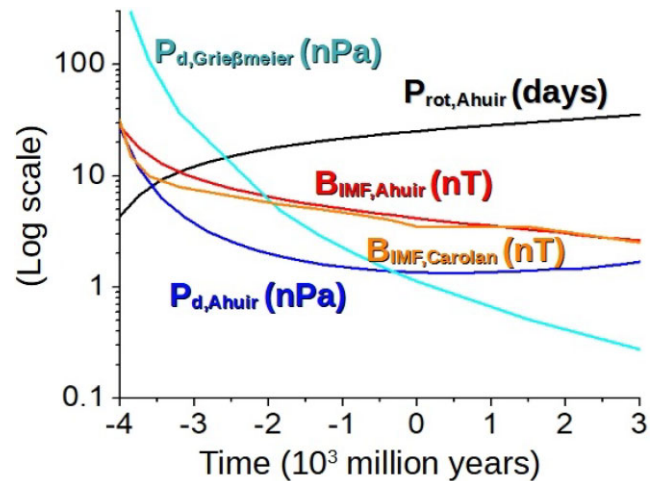


Figure 3. SW dynamic pressure by Grießmeier et al. (2007; cyan line) and by Ahuir et al. (2020; blue line) models. IMF intensity by Carolan et al. (2019; orange line) and by Ahuir et al. (2020; red line) models. Sun rotation period by Ahuir et al. (2020) model (black line).

density and temperature evolution for solar-like stars among the main sequence, coupled with a wind torque formulation consistent with the distribution of stellar rotation periods in open clusters (Reiners, Schussler & Passegger 2014; Gallet & Bouvier 2015; See et al. 2017; Jardine & Collier 2018) and the Skumanich law (Skumanich 1972, 2019) (empirical relationship between the rotation rate of a star and its age that assumes the equatorial speed of a star at its equator falls as the inverse square root of the star’s age). Fig. 3 compares the

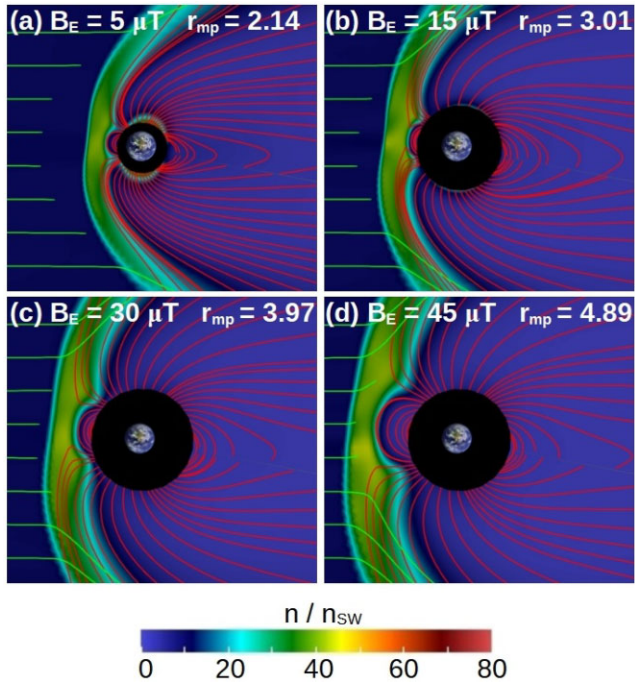


Figure 4. Polar cut of the SW density if the Earth dipole intensity is (a) 5 μT , (b) 15 μT , (c) 30 μT and (d) 45 μT . SW dynamic pressure of 50 nPa, Southward IMF intensity of 50 nT. The red lines show the Earth magnetic field and the green lines the SW velocity stream lines.

SW dynamic pressure and IMF intensity values in G-V-C and Ahuir models at different geological times. A similar prediction of the IMF intensity is observed but the Ahuir model shows a lower SW dynamic pressure before the Neo-Proterozoic and higher from the Paleozoic.

4 EARTH HABITABILITY DURING PERIODS WITH LOW AND HIGH DIPOLAR MAGNETIC FIELD STRENGTH

This section is dedicated to the analysis of the Earth habitability during periods of weak ($\leq 20 \mu\text{T}$), standard ($\sim 30 \mu\text{T}$), and high ($\geq 40 \mu\text{T}$) dipolar magnetic field intensity. The dipole model with 5 μT represents low field periods during the Proterozoic eon as well as the Cambrian, Denovian, and Carboniferous periods in the Paleozoic era and the Triassic period in the Mesozoic era (Heunemann et al. 2004; Elming et al. 2009; Hawkins et al. 2019a, 2021; Thallner et al. 2021). The dipole model with 15 μT is dedicated to study low field periods during the Paleo-Archean and Meso-Archean eras, Proterozoic eon, Jurassic period in the Mesozoic era and the Paleogene period in the Cenozoic era (Prevot et al. 1990; Kostrov et al. 1997; Morimoto et al. 1997; Juarez et al. 1998; Di Chiara et al. 2017; Calvo-Rathert et al. 2021). The dipole model with 30 μT illustrates the Meso-Proterozoic and Neo-Archean eras as well as the Neogene and Quaternary periods in the Cretaceous era (Yoshihara & Hamano 2000; Di Chiara et al. 2021; Kaya et al. 2023). The dipole model with 45 μT represents high field periods during the Hadean eon and the Eo-Archean era (Hale & Dunlop 1984; Tarduno et al. 2020).

Fig. 3 shows the Earth magnetosphere response during an ICME event with $|B|_{\text{IMF}} = 50 \text{ nT}$ and $P_d = 50 \text{ nPa}$ for a dipole model and different magnetic field intensities. The magnetopause standoff distance is located further away from the Earth surface as the dipole magnetic field intensity increases, from $r_{\text{mp}} = 2.14$ if $B_E = 5 \mu\text{T}$ to 4.89 if $B_E = 45 \mu\text{T}$. The simulations show that there is no habitability

Table 2. Regression parameters ($\log(r_{\text{mp}}) = \log(Z) + M\log(|B|_{\text{IMF}}) + N\log(P_d)$) in simulations with different SW dynamic pressure, IMF, and dipole intensity. Dipole intensity (first column), $\log(Z)$ parameter (second column), M parameter (third column), and N parameter (fourth column). The standard errors of the regression parameters are included.

B_E (μT)	$\log(Z)$	M	N
45	2.84 ± 0.03	0.141 ± 0.005	0.181 ± 0.005
30	2.55 ± 0.05	0.131 ± 0.009	0.176 ± 0.009
15	2.37 ± 0.03	0.161 ± 0.005	0.167 ± 0.004
5	2.38 ± 0.05	0.21 ± 0.01	0.204 ± 0.006

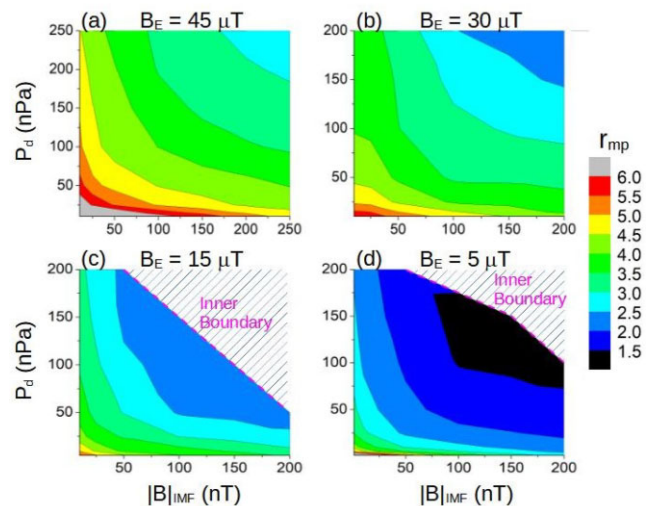


Figure 5. Isocontour of the magnetopause standoff distance for different space weather conditions if the Earth dipole magnetic field intensity is (a) 45, (b) 30, (c) 15, and (d) 5 μT .

impact caused by the SW during strong ICME events if the Earth field intensity is at least 5 μT .

Fig. 4 shows the magnetopause standoff distance for different space weather conditions (SW dynamic pressure and Southward IMF intensity) and Earth dipole magnetic field intensities. It should be recalled that the inner boundary of the simulation frame is above the Earth surface in all the models analysed, thus the simulations set cannot include space weather conditions leading to the direct precipitation of the SW towards the Earth surface. The general trend indicates a decrease of r_{mp} as P_d and B_{IMF} increase because the magnetosphere compression by the SW is higher and the Earth magnetic shield erosion by the IMF is stronger. The simulations for a dipole with 45 and 30 μT show $r_{\text{mp}} > 2.5$ in all the space weather configurations analysed, that is to say, a dipole with $\geq 30 \mu\text{T}$ can bring an adequate protection during super ICME events ($P_d = 250 \text{ nPa}$ and $B_{\text{IMF}} = 250 \text{ nT}$), stronger than the Carrington event (Carrington 1859). The simulations for a dipole with 15 and 5 μT also show $r_{\text{mp}} > 2.25$ and 1.5 during extreme space weather conditions, respectively.

Based on the parametric analysis performed, the magnetopause standoff distance is fitted with respect to P_d and $|B|_{\text{IMF}}$ by the surface function $\log(r_{\text{mp}}) = \log(Z) + M\log(|B|_{\text{IMF}}) + N\log(P_d)$. The regression provides the exponential dependency of r_{mp} with respect to the IMF intensity (M) and the SW dynamic pressure (N) as well as the proportionality constant Z . Table 2 lists the coefficients of the regressions.

Fig. 5 indicates the critical B_{IMF} values for quiet and ICME-like space weather conditions with respect to P_d (panels a and b) and time

(panels c and d) based on the G-V-C model. The needed combination of P_d and B_{IMF} to cause the direct SW deposition requires lower values as the dipole intensity decreases, particularly during ICME events. The large SW dynamic pressure in early stages of the Sun main sequence leads to a sharp decrease of the critical B_{IMF} in the Hadean eon, 0.1–340 nT for a dipole with 5 μT , $1.1\text{--}6.9 \times 10^3$ nT for a dipole with 15 μT , $1.6\text{--}140 \times 10^3$ nT for a dipole with 30 μT , and $7.4\text{--}390 \times 10^3$ nT for a dipole with 45 μT during quiet space weather conditions. ICME events cause a further decrease of the critical B_{IMF} , predicting the inability of a 5 μT dipole to protect the Earth, as well as a rather low threshold of 0.01–60 nT for a 15 μT dipole, 0.05–290 nT for a 30 μT dipole and 0.1–1050 nT for a 45 μT dipole. Consequently, the Earth habitability during the Hadean eon was strongly hampered by the space weather conditions, particularly due to the high recurrence of ICME events generated by the young Sun. Quiet space weather conditions during the Archean eon weakens compared to the Hadean eon, thus the critical B_{IMF} increases to 340– 2.5×10^3 nT for a 5 μT dipole and above 7×10^3 nT for the rest of dipole models. Nevertheless, ICME events still cause a severe decrease of the critical B_{IMF} , 4–30 nT for a 5 μT dipole, 60–500 nT for a 15 μT dipole, $290\text{--}4.6 \times 10^3$ nT for a 30 μT dipole and $1050\text{--}15 \times 10^3$ nT for a 45 μT dipole. Thus, the Earth habitability could be impacted in low field periods of the Archean Eon for ICME conditions because the lower bounds of the critical B_{IMF} are rather low in dipole models with 5 and 15 μT . There is a further mitigation of the space weather conditions along the Proterozoic eon leading to a critical B_{IMF} above 10^4 nT for all the dipole intensities tested during quiet space weather conditions. Nevertheless, ICME events can still jeopardize the Earth habitability during periods of low dipolar field because the critical B_{IMF} for the dipole model with 5 μT is 200–500 nT, larger than 4000 nT for the dipole models with ≥ 15 μT . Regarding the Phanerozoic and future eons, a dipole with an intensity of 5 μT or higher may provide an efficient shielding during quiet and ICME-like space weather conditions because the critical IMF intensity is above 700 nT, excluding super-flare events. Next, the critical B_{IMF} calculated is compared with the predicted IMF intensity at different geological times by the G-V-C model (Fig. 6). The dipole with ≥ 5 μT can protect the Earth for quiet space weather conditions during all the geological times except the Hadean eon, including the young Sun and cyclic modulations, although ICME-like space weather conditions can constrain the Earth habitability. ICME events in the Hadean eon may lead to the direct precipitation of the SW even though the dipole intensity is 45 μT . On the other hand, a dipole intensity of ≥ 30 μT may provide an efficient shielding from the Archean eon. A 15 μT dipole can only provide complete protection from the Meso-Archean era and a 5 μT dipole from the Meso-Proterozoic era. Consequently, the Earth surface and atmosphere could be exposed to the SW during ICME events in the Hadean eon and dipolar low field periods in the Paleo-Archean and Paleo-Proterozoic eras.

Fig. 7 shows the same analysis although performed using the space weather conditions predicted by the Ahuir model. Quiet space weather conditions are not included in the discussion because there is no strong impact on the Earth habitability. The analysis shows some differences compared to G-V-C model results. In particular, the analysis based on Ahuir model indicates a 45 μT dipole can protect the Earth during the Hadean eon, unprotected based on G-V-C model. Likewise, 15 and 5 μT dipoles provides an efficient shielding from the Eo-Archean and Paleo-Proterozoic eras, respectively, although G-V-C model delay the magnetosphere protection to the Meso-Archean and Meso-Proterozoic eras. The deviation between models results

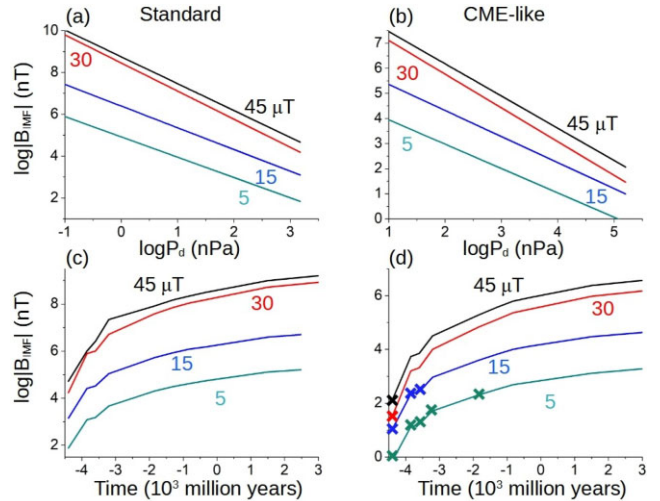


Figure 6. Critical Southwards IMF intensity required in G-V-C model for the direct deposition of the SW towards the Earth surface during quiet space weather conditions with respect to the (a) SW dynamic pressure and (b) geological time. Same study for ICME-like space weather conditions with respect to (b) SW dynamic pressure and (d) geological time. The black line indicates the dipole model with 45 μT , the red line for 30 μT , the blue line for 15 μT , and the cyan line for 5 μT . The bold crosses indicate the geological times the SW may jeopardize the Earth’s habitability for each magnetic field configuration.

is caused by a lower SW dynamic pressure estimation in the Ahuir model before the Neo-Proterozoic.

In summary, habitability constraints caused by the SW during the Hadean eon did not affect the life evolution because the Earth was inhospitable to any organisms, showing acid boiling oceans and an atmosphere rich in carbon dioxide as well as the continuous bombardment of asteroids and comets (Kasting 1993; Morse & Mackenzie 1998; Dodd et al. 2017). On the other hand, the erosion caused by the SW on the primary Earth atmosphere could enhance the water molecules escape as well as the fast hydrogen and helium exhaust by increasing the leak ratios (Kasting 2014; Thomassot et al. 2015; Shaw 2019). SW sterilizing effect during the Paleo-Archean may have an effect on the emerging life such as microbial mats and bacteria (Lepot 2020) as well as on the atmosphere evolution (Catling & Zahnle 2020). Same discussion can be done for the Meso-Proterozoic era, particularly about the effect of the SW on the outbreak of complex life forms as multicellular organisms (Butterfield 2000) and the atmosphere early oxygenation (Parnell et al. 2010).

5 EARTH HABITABILITY DURING PERIODS WITH MULTIPOLAR MAGNETIC FIELD

This section is dedicated to study the Earth habitability during periods of weak multipolar fields linked to geomagnetic reversals (McElhinny 1971; Bogue & Merrill 1992; Gubbins 2008). Polarity inversions lead to a weakening of the Earth magnetic shield thus weaker space weather conditions are required for the SW direct precipitation towards the surface (Glatzmaiers & Roberts 1995). For example, paleomagnetic data revealed a large quadrupolar component of the Earth magnetic field along the Proterozoic age as well as the Devonian and Cretaceous periods (Guyodo & Valet 1999; Lhuillier et al. 2016; Shcherbakova et al. 2017). There is a limited amount of information about the magnetic field topology

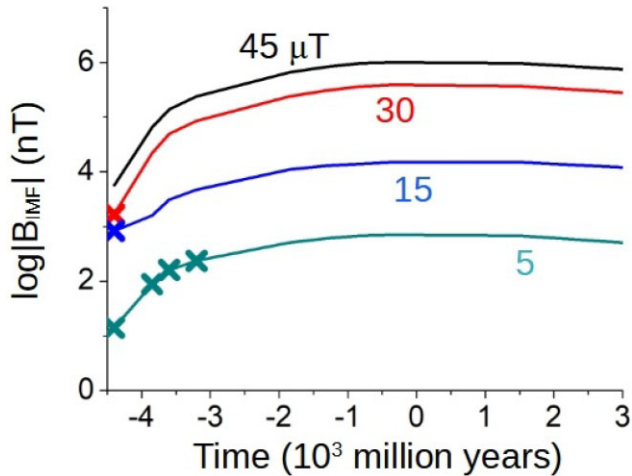


Figure 7. Critical Southwards IMF intensity required in Ahuir model for the direct deposition of the SW towards the Earth surface during ICME-like space weather conditions for a dipolar magnetic field configuration. black line 45 μT , red line 30 μT , blue line 15 μT , and cyan line 5 μT . The bold crosses indicate the geological times the SW may jeopardize the Earth habitability for each magnetic field configuration.

during geomagnetic reversals (Valet et al. 2012; Valet & Fournier 2016), thus the effect of the space weather on the habitability is modeled using four different configurations, multipolar fields with quadrupole to dipole coefficient ratios of 0.2 and 0.5 for a field intensity of 5 and 15 μT at the equatorial region of the Earth surface. Consequently, the simulations results can be directly compared with the dipolar models with 5 and 15 μT .

Fig. 8 shows the deformation of the Earth magnetosphere caused by a common ICME ($P_d = 10$ nPa and $B_{\text{IMF}} = 10$ nT) during a dipolar low field period, panel a, and a multipolar low field period with $Q/D = 0.5$, panel b, if the field intensity is 15 μT . The magnetic field lines (red lines) show clear differences in the magnetosphere topology and the SW deflection by the magnetic shield (green lines indicate the SW velocity stream lines). Consequently, the magnetopause standoff distance is different, $r_{\text{mp}} = 4.9$ in the dipole model and 2.9 in the multipolar model, pointing out a rather large decrease of r_{mp} in the multipolar case compared to the dipole model. That means a multipolar Earth magnetic field is strongly constrained by the space weather conditions and the Earth habitability easily hampered.

Fig. 9 shows the magnetopause standoff distance for different space weather conditions, Earth magnetic field quadrupole to dipole coefficient ratios and intensities. If the panels (a) and (b) are compared with the Fig. 4(c), there is a decrease of r_{mp} as the Q/D ratio increases for the same space weather conditions, particularly as the ICME events are more severe. The same discussion can be done comparing panels (c) and (d) with the Fig. 4(d). In addition, the multipolar model with 15 μT $Q/D = 0.2$ shows r_{mp} values 15 per cent larger in averaged compared to the dipolar case with 5 μT for the same space weather conditions, reduced to 11 per cent for the multipolar model with 15 μT $Q/D = 0.5$. Consequently, for the same Earth magnetic field intensity, configurations with a larger Q/D ratio lead to a lower magnetopause stand off distance. Indeed, ICME-like space weather conditions leads to $r_{\text{mp}} < 2.0$, thus the Earth habitability is more hampered in the multipolar models with respect to the dipole model.

Next, r_{mp} values calculated in the parametric analysis are fitted using the same surface function of Section 4. Table 3 indicates the coefficients of the regressions.

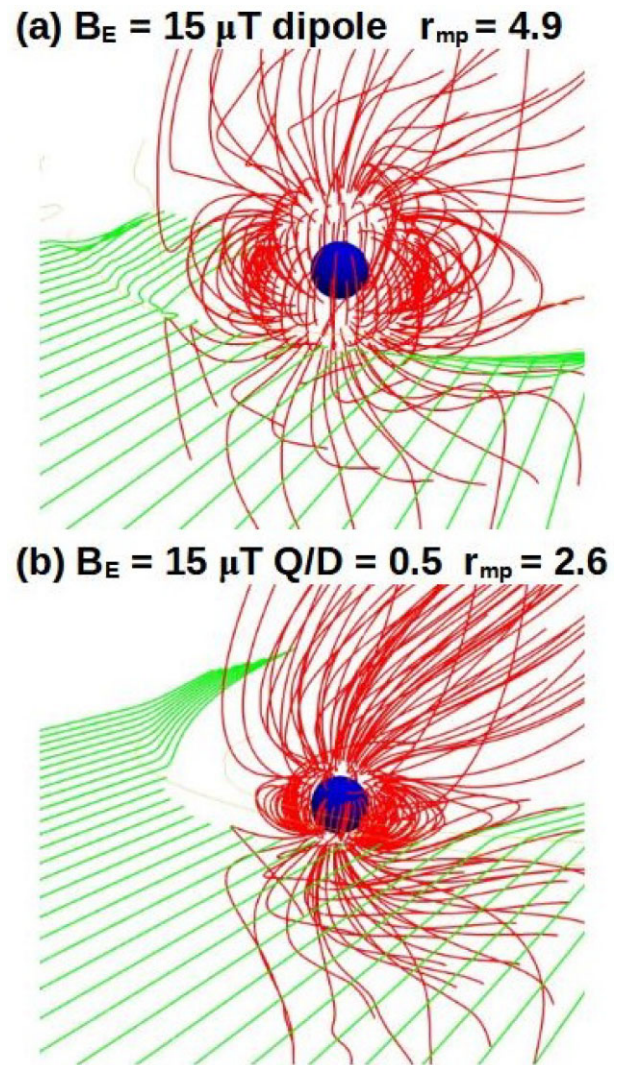


Figure 8. 3D view of the Earth magnetosphere for (a) dipole and (b) multipolar $Q/D = 0.5$ models with a magnetic field intensity of 15 μT . Earth magnetic field lines (red lines) and SW velocity stream lines (green lines).

Table 3. Regression parameters ($\log(r_{\text{mp}}) = \log(Z) + M\log(|B|_{\text{IMF}}) + M\log(P_d)$) in simulations with different SW dynamic pressure, IMF intensity, Q/D ratio, and Earth magnetic field intensity. Q/D ratio (first column), Earth magnetic field intensity (second column), $\log(Z)$ parameter (third column), M parameter (fourth column), and N parameter (fifth column). The standard errors of the regression parameters are included.

Q/D	B_E (μT)	$\log(Z)$	M	N
0.2	15	1.95 ± 0.06	0.175 ± 0.013	0.144 ± 0.008
0.5	15	1.88 ± 0.04	0.164 ± 0.009	0.151 ± 0.005
0.2	5	1.52 ± 0.07	0.18 ± 0.02	0.13 ± 0.01
0.5	5	1.58 ± 0.06	0.201 ± 0.013	0.172 ± 0.011

Again, the critical B_{IMF} required for the direct SW deposition is calculated based on the SW velocity and density estimation at the Earth orbit along the Sun's evolution on the main sequence by G-V-C model. Fig. 9 shows the critical B_{IMF} values for quiet and ICME-like space weather conditions with respect to P_d and time. The critical B_{IMF} in the Hadean eon during quiet space weather

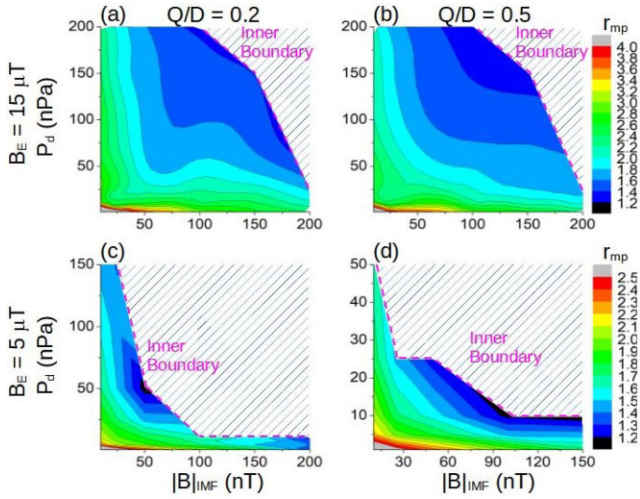


Figure 9. Isocontour of the magnetopause standoff distance for different space weather conditions if (a) $Q/D = 0.2$ and $B_E = 15 \mu\text{T}$, (b) $Q/D = 0.5$ and $B_E = 15 \mu\text{T}$, (c) $Q/D = 0.2$ and $B_E = 5 \mu\text{T}$, and (d) $Q/D = 0.5$ and $B_E = 5 \mu\text{T}$.

conditions for the models with $5 \mu\text{T}$ $Q/D = 0.2$ and 0.5 is $0.2\text{--}80$ and $0.1\text{--}20$ nT, respectively. On the other hand, the Earth is completely exposed to the SW during ICME events. The models with $15 \mu\text{T}$ $Q/D = 0.2$ and 0.5 show an increase of the critical B_{IMF} by one order of magnitude compared to $5 \mu\text{T}$ cases for quiet space weather conditions, $1\text{--}520$ nT, although the critical B_{IMF} is rather lower during ICMEs, ≤ 0.1 nT. Consequently, multipolar low fields cannot protect the Earth during the Hadean eon. A more tempered space weather in the Archean eon lead to an increase of the critical B_{IMF} to $20\text{--}120$ nT for the model with $5 \mu\text{T}$ $Q/D = 0.5$ and to $80\text{--}345$ nT for the $5 \mu\text{T}$ $Q/D = 0.2$ case during quiet conditions. The critical B_{IMF} is below 50 nT during ICME events so multipolar $5 \mu\text{T}$ models cannot provide an efficient magnetic shield. Same discussion can be done for the $15 \mu\text{T}$ models, enough to protect the Earth during quiet space weather condition, critical B_{IMF} ranges between 1 and 3425 nT, although decreasing to values $\leq 1\text{--}50$ nT during ICME events. Thus, multipolar low fields may not be able to protect the Earth during the Archean eon neither. Proterozoic and Phanerozoic eons show critical B_{IMF} values above 660 nT for both $5 \mu\text{T}$ models during quiet space weather conditions. The lower-upper bounds during ICME-events is $15\text{--}46$ nT in the model with $Q/D = 0.5$ and $53\text{--}154$ nT if $Q/D = 0.2$, thus multipolar low fields with $5 \mu\text{T}$ may not protect the Earth during strong ICME events even in the present days. On the other hand, $15 \mu\text{T}$ models may provide an efficient shield during quiet and ICME events. Regarding Postterum eons, multipolar fields with $15 \mu\text{T}$ $Q/D \leq 0.5$ and $5 \mu\text{T}$ $Q/D \leq 0.2$ can protect the Earth, critical $B_{\text{IMF}} \approx 270$ nT, although $\leq 5 \mu\text{T}$ $Q/D \geq 0.5$ magnetic fields may not provide an efficient shielding for Carrington-like events with a critical $B_{\text{IMF}} \approx 90$ nT. Now, the critical B_{IMF} is compared with the predicted B_{IMF} values along the Sun's evolution on the main sequence by the G-V-C model (Fig. 10). Quiet space weather conditions can only hamper the Earth habitability during the Hadean eon if the multipolar magnetic field intensity is $\leq 15 \mu\text{T}$. ICME events could constrain the Earth habitability in the Archean eons as well as in the Paleo-Proterozoic era during multipolar field periods with $B_E \leq 15 \mu\text{T}$ and $Q/D \geq 0.2$. From the Meso-Proterozoic era multipolar fields with $15 \mu\text{T}$ and $Q/D \leq 0.5$ provide an efficient magnetic shield, just like a multipolar field with $5 \mu\text{T}$ and $Q/D \leq 0.2$ in Postterum eons. Only the multipolar

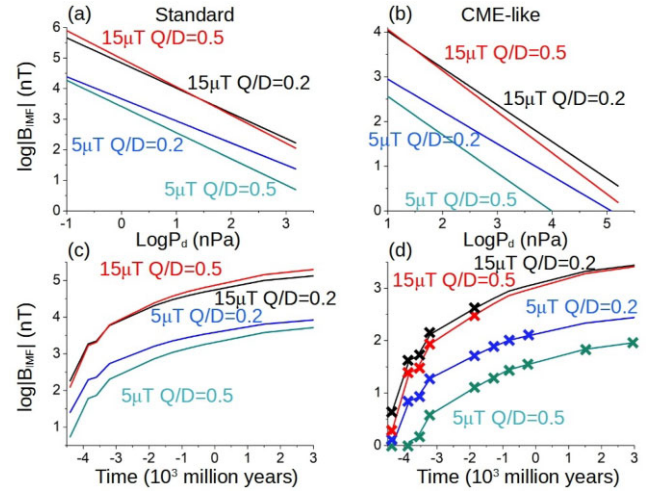


Figure 10. Critical Southwards IMF intensity required in G-V-C model for the direct deposition of the SW towards the Earth surface during quiet space weather conditions with respect to the (a) SW dynamic pressure and (c) geological time. Same study for ICME-like space weather conditions with respect to the (b) SW dynamic pressure and (d) geological time. The black line indicates the model with $Q/D = 0.2$ and $15 \mu\text{T}$, the red line for $Q/D = 0.5$ and $15 \mu\text{T}$, the blue line for $Q/D = 0.2$ and $5 \mu\text{T}$, and the cyan line for $Q/D = 0.5$ and $5 \mu\text{T}$. The bold crosses indicate the geological times the SW may jeopardize the Earth habitability for each magnetic field configuration.

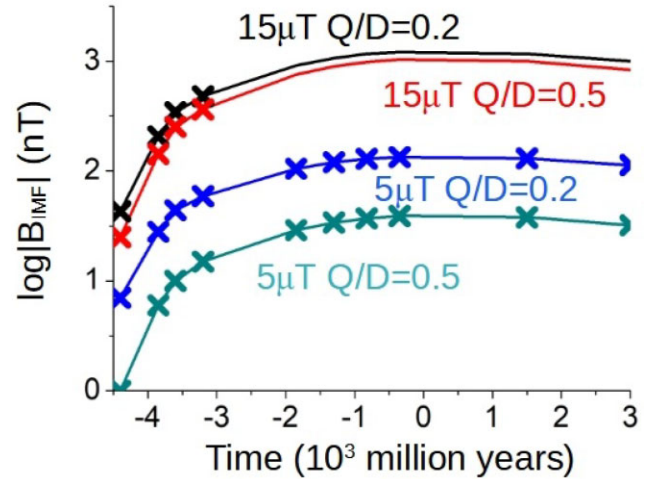


Figure 11. Critical Southwards IMF intensity required in Ahuir model for the direct deposition of the SW towards the Earth surface during ICME-like space weather conditions for a multipolar Earth magnetic field configuration: black line $Q/D = 0.2$ and $15 \mu\text{T}$, red line $Q/D = 0.5$ and $15 \mu\text{T}$, blue line $Q/D = 0.2$ and $5 \mu\text{T}$, and cyan line $Q/D = 0.5$ and $5 \mu\text{T}$. The bold crosses indicate the geological times the SW may jeopardize the Earth habitability for each magnetic field configuration.

fields with $5 \mu\text{T}$ and $Q/D \geq 0.2$ are unable to protect the Earth in the Paleozoic era and Postterum eons.

Fig. 11 shows the analysis results based on Ahuir space weather predictions. A multipolar field with $15 \mu\text{T}$ and $Q/D \leq 0.5$ can protect the Earth from the Paleo-Proterozoic era based on Ahuir model (from the Meso-Proterozoic era based on G-V-C models) because the predicted SW dynamic pressure is lower. On the other hand, a multipolar field with $5 \mu\text{T}$ and $Q/D \geq 0.2$ cannot shield the Earth during any geological time using Ahuir model, unlike the G-V-C

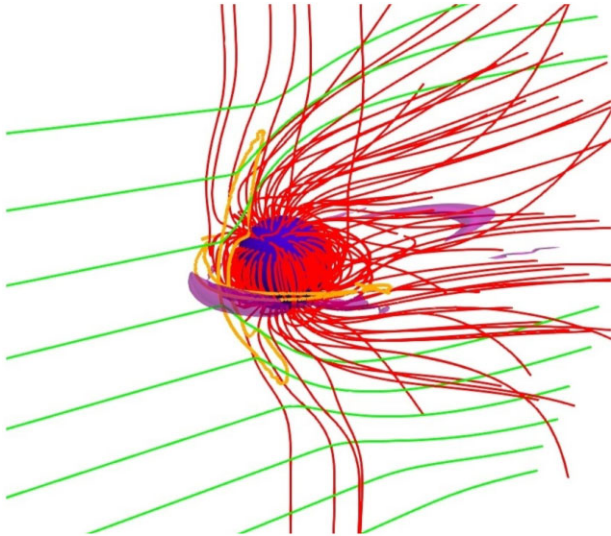


Figure 12. 3D view of the Earth magnetosphere topology for a dipole $0.1 \mu\text{T}$ during quiet space weather conditions (Southward $B_{\text{IMF}} = 1 \text{ nT}$ and $P_{\text{d}} = 1 \text{ nPa}$). Earth magnetic field lines (red lines), SW velocity stream lines (green lines), isoline of the plasma density for $n/n_{\text{sw}} = 30$ in the XY and XZ planes (bold orange lines), and reconnection region between the IMF and the Earth magnetic field (pink iso-volume.).

models that show an efficient protection from the Paleozoic for the configuration with $Q/D \leq 0.2$. Such difference is explained by an increment of the SW dynamic pressure from the Paleozoic eon in Ahuir model, leading to a larger SW dynamic pressure with respect to the G-V-C models from the Neo-Proterozoic era.

The analysis of the multipolar low field periods confirms the discussion initiated in Section 4 about the Earth vulnerability during geomagnetic reversals. Multipolar low field periods may lead to an enhanced atmosphere erosion during the Hadean and Archean eons as well as the Paleo-Proterozoic era. Also, multipolar low field periods with $B_{\text{E}} \leq 5 \mu\text{T}$ during the Proterozoic eon could affect the incipient multicellular organisms. It should be noted that multipolar low field periods with $B_{\text{E}} \leq 5 \mu\text{T}$ and $Q/D \geq 0.5$ are unable to protect the Earth in the Phanerozoic eon, that is to say, the Earth habitability can be jeopardized during geomagnetic reversals in the present time. Indeed, several studies link mass-extinction in the Phanerozoic eon with geomagnetic reversal periods (Kennett & Watkins 1970; Plotnick 1980; Worm 1997; Isozaki 2009; Wei et al. 2014; Isozaki & Servais 2018), particularly for the Late Devonian (McGhee 1988; Hawkins et al. 2019b; van der Boon et al. 2022) (372 million years ago), Permian–Triassic (251.9 million years ago; Benton & Twitchett 2003; Poreda & Becker 2003; Heunemann et al. 2004; Onoue et al. 2019), and Triassic–Jurassic (201.4 million years ago; van Zijl, Graham & Hales 1962; Wei et al. 2014; Schoepfer et al. 2022) extinction events.

6 EARTH HABITABILITY IN POSTERUM EONS: DECAYING DIPOLE

The last section of the study is dedicated to analyse the effect of the SW on the Earth habitability in Posterum eons, once the geodynamo begins to fade away as well as the Earth magnetic field. Numerical models predict a decay of the Earth magnetic field as the Earth core cools down and expands leading to the eventual termination of the geodynamo, a process that occurred several 1000 million years ago in Mars (Roberts & Glatzmaier 2001; Roberts,

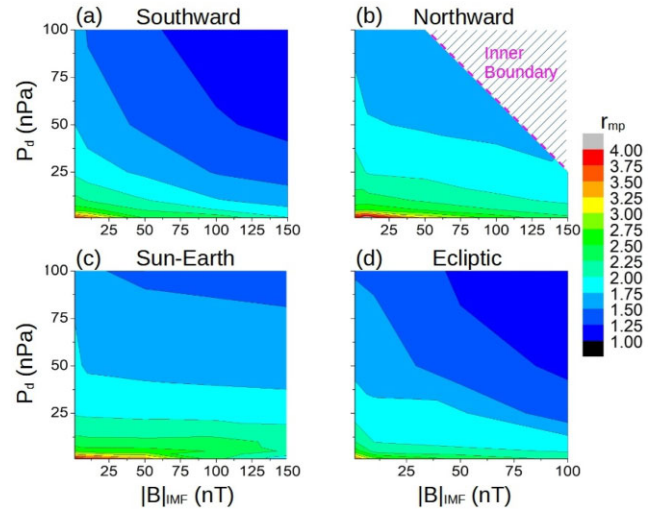


Figure 13. Isocontour of the magnetopause standoff distance for different space weather conditions if the Earth dipole intensity is $1 \mu\text{T}$ and the IMF orientation is (a) Southward (b) Northward, (c) Sun–Earth, and (d) Ecliptic.

Lillis & Manga 2009; Jones 2011; Smirnov et al. 2017). Geodynamo simulations predict large non dipolar components of the Earth magnetic field during the decay phase (Roberts & Glatzmaier 2001), thus the analysis is connected with the multipolar models studied in the previous section that already identified a vulnerable Earth habitability during ICME-like events if $B_{\text{E}} \leq 5 \mu\text{T}$ and $Q/D \geq 0.5$. Consequently, a further decrease of the Earth magnetic field intensity or an increase of the Q/D ratio along Posterum eons could cause an inefficient magnetic shielding not only during ICME event, also for quiet space weather conditions. Such hypothetical configurations are explored performing a new set of simulations assuming Earth dipolar fields with 1 and $0.1 \mu\text{T}$, providing the upper bound of the Earth habitability with respect to multipolar models for the same field intensity. In addition, the analysis is extended to include different IMF orientations, particularly the Sun–Earth or radial IMF (parallel to the SW velocity vector), Northward and Southward IMF (perpendicular to the SW velocity vector at the XZ plane), and ecliptic counterclockwise IMF.

Fig. 12 shows the Earth magnetosphere during quiet space weather conditions ($P_{\text{d}} = 1 \text{ nPa}$ and Southward $B_{\text{IMF}} = 1 \text{ nT}$) if the Earth dipole intensity is $0.1 \mu\text{T}$. The magnetopause standoff distance is 1.44, that is to say, the Earth magnetic field (red lines) can barely deflect the SW (green lines) thus the bow show (orange lines) and the reconnection region between IMF and Earth magnetic field (pink iso-volume) are located close to the Earth surface. Consequently, the Earth surface and atmosphere could be exposed to the SW as soon as there is a small increase of the SW density/velocity or the IMF intensity.

Figs 13 and 14 show the magnetopause standoff distance for different space weather conditions and dipole models with 1 and $0.1 \mu\text{T}$, respectively. The erosion caused by a Southward IMF in the Earth magnetic field leads to the configurations with the lowest r_{mp} . On the other hand, a Northward IMF enhances the Earth magnetic field in the equatorial region leading to the configuration with the largest r_{mp} . The Sun–Earth IMF erodes the Earth magnetic field in the Southward hemisphere and the ecliptic IMF induces a magnetosphere East–West tilt, leading to configuration showing intermediate r_{mp} values compared to the Southward and Northward IMF cases. Dipole model simulations with $1 \mu\text{T}$ show $r_{\text{mp}} > 1$ for space weather configurations

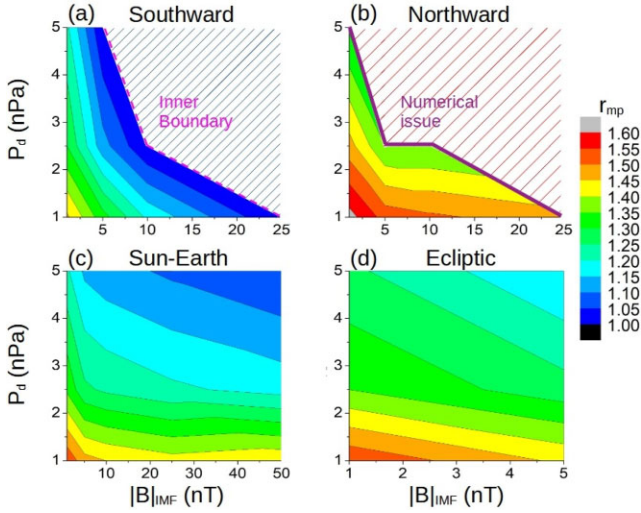


Figure 14. Isocontour of the magnetopause standoff distance for different space weather conditions if the Earth dipole intensity is $0.1 \mu\text{T}$ and the IMF orientation is (a) Southward (b) Northward, (c) Sun-Earth, and (d) Ecliptic.

Table 4. Regression parameters ($\log(r_{\text{mp}}) = \log(Z) + M\log(|B_{\text{IMF}}|) + N\log(P_d)$) in simulations with different SW dynamic pressure, IMF intensity and orientation as well as Earth magnetic field intensity. Earth magnetic field intensity (first column), IMF orientation (second column), $\log(Z)$ parameter (third column), M parameter (fourth column), and N parameter (fifth column). The standard errors of the regression parameters are included.

B_E (μT)	IMF	$\log(Z)$	M	N
1	Southward	1.55 ± 0.04	0.119 ± 0.0008	0.194 ± 0.008
1	Northward	1.32 ± 0.05	0.054 ± 0.009	0.150 ± 0.009
1	Earth-Sun	1.31 ± 0.04	0.024 ± 0.007	0.180 ± 0.007
1	Ecliptic	1.32 ± 0.09	0.08 ± 0.02	0.17 ± 0.02
0.1	Southward	0.36 ± 0.03	0.088 ± 0.013	0.10 ± 0.02
0.1	Northward	0.485 ± 0.012	0.032 ± 0.005	0.13 ± 0.01
0.1	Earth-Sun	0.441 ± 0.008	0.045 ± 0.003	0.166 ± 0.005
0.1	Ecliptic	0.433 ± 0.008	0.045 ± 0.005	0.133 ± 0.007

with $P_d \leq 100 \text{ nPa}$ and $B_{\text{IMF}} \leq 100 \text{ nT}$ for all the IMF orientations. On the other hand, if the dipole intensity is $0.1 \mu\text{T}$, configurations leading to $r_{\text{mp}} > 1$ requires P_d and B_{IMF} values not much higher than quiet space weather conditions.

The r_{mp} values calculated for the dipole model with 1 and $0.1 \mu\text{T}$ are fitted using the same surface function of Section 4. The regression results are shown in the Table 4.

Fig. 15 shows the critical B_{IMF} values for ICME-like space weather conditions with respect to P_d and time in the Posterum eons based on the G-V-C model. Quiet space weather conditions are not included in the analysis because there is no impact on the Earth habitability (parametric region highlighted by the light blue rectangle in panel a). The critical B_d calculated for a dipole with $0.1 \mu\text{T}$ during ICME events (yellow rectangle in panel a) is smaller than 1 nT for all the IMF orientation tested. On the other hand, the critical B_d for a dipole with $1 \mu\text{T}$ is 750 nT for a Southward IMF, and $> 10^4 \text{ nT}$ for the other IMF orientations. Now, the critical B_{IMF} calculated for different IMF orientations is compared with the predicted B_{IMF} values. If the dipole intensity is $\leq 1 \mu\text{T}$, a Southward IMF orientation can impact the Earth habitability in present and Posterum eons although a dipole with $1 \mu\text{T}$ is strong enough to shield the Earth for all the other IMF orientations analyzed. On the other hand, a dipole with

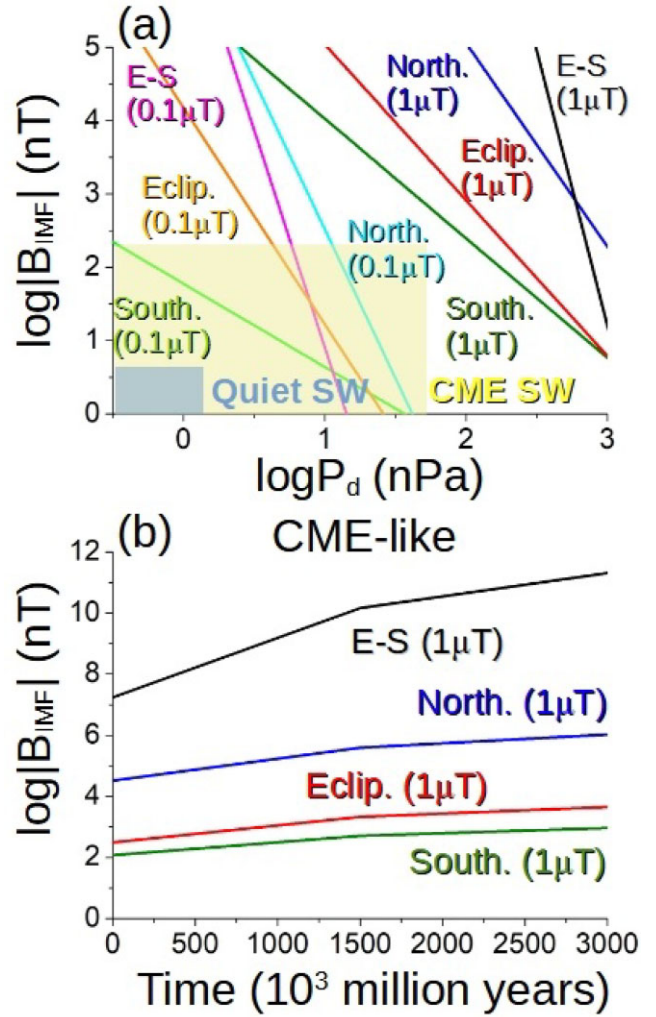


Figure 15. Critical IMF intensity required in the G-V-C model for the direct deposition of the SW towards the Earth surface during ICME space weather conditions with respect to the (a) SW dynamic pressure and (b) geological time (Posterum eons). The green (light green) line indicates the model with $B_E = 1$ ($0.1 \mu\text{T}$) and Southward IMF, the red (orange) line the model with $B_E = 1$ ($0.1 \mu\text{T}$) and Ecliptic IMF, the blue (cyan) line the model with $B_E = 1$ ($0.1 \mu\text{T}$) and Northward IMF, the light black (pink) line indicates the model with $B_E = 0.1$ ($0.1 \mu\text{T}$) and Earth-Sun IMF. The bold crosses indicate the geological times the SW may jeopardize the Earth habitability for each magnetic field configuration.

$0.1 \mu\text{T}$ cannot protect the Earth for any of the IMF orientations tested.

Fig. 16 shows the analysis results based on Ahuir space weather predictions. The results are very similar compared to the G-V-C model, no impact on the Earth habitability for all the IMF orientations during quiet space weather conditions if the dipole intensity is $\geq 0.1 \mu\text{T}$. On the other hand, the Earth habitability can be jeopardized during ICME events if the dipole intensity is $\leq 0.1 \mu\text{T}$ for all the IMF orientations analysed. Only one discrepancy is observed with the G-V-C model results, because the analysis based on the Ahuir models shows ICME-like space weather conditions do not impact the Earth for any of the IMF analysed if the dipole intensity is $\geq 1 \mu\text{T}$.

In summary, the analysis shows the Earth habitability could be hampered in Posterum eons during ICME-like space weather

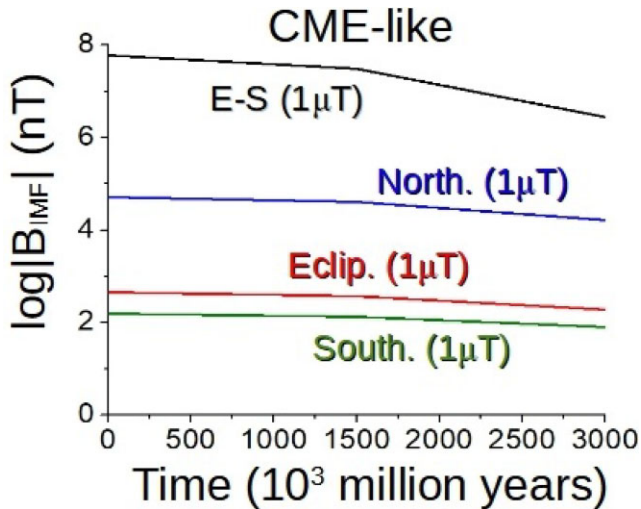


Figure 16. Critical IMF intensity required in the Ahur model for the direct deposition of the SW towards the Earth surface during ICME space weather conditions with respect to the geological time (Posterior eons). The green (light green) line indicates the model with $B_E = 1$ (0.1) μT and Southward IMF, the red (orange) line the model with $B_E = 1$ (0.1) μT and Ecliptic IMF, the blue (cyan) line the model with $B_E = 1$ (0.1) μT and Northward IMF, the light black (pink) line indicates the model with $B_E = 0.1$ (0.1) μT , and Earth–Sun IMF.

conditions if the dipole intensity decreases below 1 μT , particularly if the IMF is Southward. This result complements the identification of a direct SW precipitation during geomagnetic reversals obtained in the previous section for multipolar magnetic fields with ≤ 5 μT and $Q/S \geq 0.5$. In addition, if the dipole intensity is ≤ 0.1 μT , the Earth is barely protected during quiet space weather conditions.

7 IONOSPHERE EXPANSION: CONSEQUENCE FOR THE EARTH HABITABILITY

EUV and X-ray fluxes in the Hadean and Archean eons were much larger compared to the present because the Sun was a more active star (Ribas et al. 2005; Tu et al. 2015). Decay laws predict a decrease of the X-ray fluxes by a factor of 1000–200, EUV around hundreds and UV by a factor of 10 along the Sun main sequence (Guinan & Ribas 2002; Ribas et al. 2005). For example, observations by Guinan & Ribas (2002) show X-ray fluxes decrease from 3 to 0.02 $\text{erg s}^{-1} \text{cm}^{-2} \text{\AA}^{-1}$ comparing star with ages of 130 and 750 Mya, further reduced to $10^{-4} \text{erg s}^{-1} \text{cm}^{-2} \text{\AA}^{-1}$ if the star age is 1600 Mya. Likewise, EUV fluxes decay from 0.3 to 0.04 $\text{erg s}^{-1} \text{cm}^{-2} \text{\AA}^{-1}$ between stars with ages of 130 and 750 Mya, around 0.004 $\text{erg s}^{-1} \text{cm}^{-2} \text{\AA}^{-1}$ if the star age is 1600 Mya. EUV and X-ray radiation are absorbed in the atmosphere upper layers leading to an enhancement of the gas ionization and heating (Tian et al. 2008a, b; Johnstone et al. 2021a). Consequently, the upper atmosphere and ionosphere expanded beyond several Earth radius (Lammer et al. 2018), effect also observed in the ionosphere of Mars and Venus (Dubinin et al. 2019; Han et al. 2020).

The expansion of the upper atmosphere/ionosphere had several consequences, for example an increase of the ions (Lichtenegger et al. 2010; Kislyakova et al. 2020) and neutrals (Tian et al. 2008a, b; Johnstone et al. 2021a) loss rates as well as affecting the bow shock and magnetopause standoff distances. That means, the analysis of the Earth habitability with respect to the SW direct deposition in the

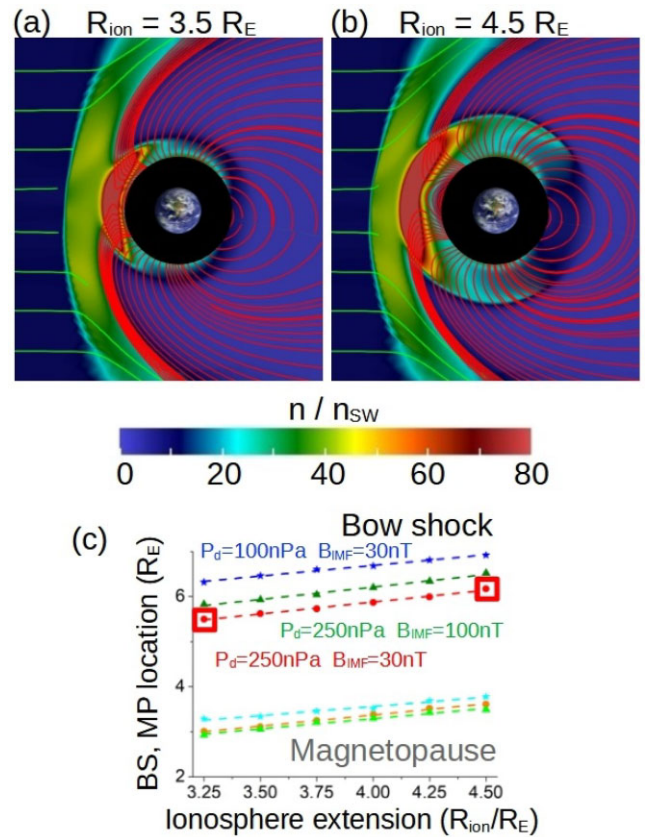


Figure 17. Polar cut of the SW density if the ionosphere extension is (a) 6400 km and (b) 12 740 km. SW dynamic pressure of 250 nPa, Southward IMF intensity of 30 nT. The red lines show the Earth magnetic field and the green lines the SW velocity stream lines. (c) Bow shock (r_{bs}) and magnetopause (r_{mp}) standoff distances for different ionosphere extensions (R_{ion}) and space weather conditions: $P_d = 250$ nPa and $B_{IMF} = 30$ nT (red BS and orange MP), $P_d = 100$ nPa and $B_{IMF} = 30$ nT (blue BS and cyan MP) and $P_d = 250$ nPa and $B_{IMF} = 100$ nT (green BS and light green MP). Red squares indicate the cases plotted in panels (a) and (b).

Hadean and Archean eons requires adding the effect of the ionosphere expansion to improve the model accuracy.

The ionosphere expansion is introduced in the simulations by modifying the ionosphere model (please see the appendix for further information). In this first attempt, the direct modelling of EUV and X-ray forcing is not included in a self consistent manner, a task that will be performed in a future work. In addition, the analysis implicitly assumes an averaged effect of the different radiation wavelengths on the ionosphere expansion (Paul, Strugarek & Vaidya, in preparation; Gillet, Garcia-Muñoz & Strugarek, in preparation). The extended model can evaluate the effect of the ionosphere expansion on the bow shock and magnetopause standoff distance. A set of simulations are performed dedicated to analyze an ionosphere expanded from $R = 2.5R_E$ to $R = 3.0R_E + i \cdot 0.25R_E$ with $i = [1, 6]$, that is to say, ionosphere extensions from 12 740 to 4780 km representing the Earth ionosphere evolution from the Hadean to the Archean eon as the EUV and X-ray fluxes decays as the Sun evolves along the main sequence (Ribas et al. 2005). The ionosphere extension is defined as R_{ion} , Fig. 17, panels (a) and (b), show the bow shock and Earth magnetic field lines in the polar plane in simulations with an ionosphere expanded from 2.5 to $3.5R_E$ and from 2.5 to $4.5R_E$, respectively, if $P_d = 250$ nPa and $B_{IMF} = 30$ nT. The bow shock and magnetopause standoff

Table 5. Regression parameters ($r_{\text{mp,bs}} = A + BR_{\text{ion}}$) in simulations with different space weather conditions. The standard errors of the regression parameters are included.

Case (P_d nPa, B_{IMF} nT)	Bow shock		Magnetopause	
	A	B	A	B
100,30	4.80 ± 0.06	0.47 ± 0.02	1.94 ± 0.12	0.41 ± 0.03
250,30	3.78 ± 0.08	0.53 ± 0.02	1.38 ± 0.06	0.50 ± 0.02
250,100	4.00 ± 0.11	0.55 ± 0.03	1.47 ± 0.10	0.46 ± 0.03

distances increase as the ionosphere expands. Panel (c) indicates the bow shock and magnetopause standoff distances calculated for different ionosphere extensions and space weather conditions. The analysis indicates the standoff distance increases as the ionosphere expands. The linear fit $r_{\text{MP,BS}} = A + BR_{\text{ion}}$ is calculated using the bow shock and magnetopause standoff distance with respect to the ionosphere extension. The regression parameters are in Table 5. The ratio between standoff distances and R_{ion} is similar for all the cases tested, and averaged ratio of 0.52 for the bow shock and 0.46 for the magnetopause. It should be noted that the simulation results may depend on the IMF orientation, thus a detail characterization requires a more extended analysis out of the scope of the present study. Nevertheless, the simulations already indicate the standoff ratio depends on the bow shock and Earth magnetic field compression induced by the SW dynamic pressure as well as the IMF intensity. The effect of the magnetosphere compression is observed comparing configurations with the same B_{IMF} although different P_d : the case with 250 nPa (red-orange) shows lower standoff distances compared to the configuration with 100 nPa (blue-cyan). Also, the standoff ratio is larger in the case with 250 nPa because bow shock and magnetopause are closer to the ionosphere and the effect of the ionosphere expansion is larger. The effect of the IMF intensity is analysed comparing configurations with the same P_d and different B_{IMF} . The case with 100 nT shows a lower magnetopause standoff distance with respect to the case with 30 nT, caused by a stronger erosion of the Earth magnetic field in the equatorial region. However, the bow shock standoff distance is larger in the case with 100 nT because the magnetic field intensity in the bow shock region is almost three times higher compared to the 30 nT case, that is to say, the accumulation of IMF lines leads to a further extension of the bow shock.

In summary, the Earth magnetosphere expansion induced by EUV and X-ray fluxes, hundreds to thousand times larger during the Hadean and Archean eons compared to the present time, leads to an increase of the bow shock and magnetopause standoff distance, reducing the habitability constraints imposed by the SW. On the other hand, the large SW dynamic pressure in the Hadean and Archean eons partially counterbalance the ionosphere expansion, leading to a stronger ionosphere compression that may explain why the standoff distance ratio calculated in the simulations ranges between 0.41 and 0.55 for the different space weather conditions analysed. Thus, any further increase of the SW dynamic pressure causes a stronger compression of the ionosphere, opposing the ionosphere expansion and the increase of the bow shock and magnetopause standoff distance. It should be noted that the IMF lines pile up in the bow shock region causes a further extension of the bow shock standoff distance as the IMF intensity increases while the magnetopause standoff distance decrease, particularly in configurations with Southward IMF orientation. Consequently, the set of simulations performed ignoring the effect of the ionosphere expansion during the Hadean and Archean eons provides a lower bound of the standoff distance, that is to say, the Earth habitability constraints are less restrictive

at least for quiet space weather configurations. It should be recalled that, simulations without the effect of the ionosphere expansion for quiet space weather conditions during the Hadean and Archean eons already predict an efficient shielding by the Earth magnetic field. That means, adding the effect of the ionosphere expansion does not change the study conclusions. However, CME-like space weather conditions should be analysed in more detail and should include the ionosphere expansion to provide a more accurate prediction of the SW P_d and B_{IMF} threshold for a direct SW precipitation on the Earth surface. Such analysis will be the topic of future analysis.

8 DISCUSSION AND CONCLUSIONS

The Earth habitability states caused by the solar wind along the Sun's evolution on the main sequence are analysed considering the evolution of the space weather conditions as well as different Earth magnetic field intensities and topologies inferred from paleomagnetism surveys and numerical models. The study is based on a set of simulations performed with the MHD code PLUTO, calculating the magnetopause standoff distance resulting for different space weather conditions (parametrized by the solar wind dynamic pressure and the intensity of a Southward IMF) and Earth magnetic field models (intensity and quadrupole–dipole coefficient ratios). The data set obtained for the magnetopause standoff distance is fitted with respect to the surface function $\log(r_{\text{mp}}) = \log(Z) + M\log(|B_{\text{IMF}}|) + N\log(P_d)$ and compared to the SW dynamic pressure and IMF intensity along the Sun's evolution on the main sequence obtained from the models by Griebmeier et al. (2007), Vidotto et al. (2014), Carolan et al. (2019), and alternatively with Ahuir et al. (2020) model. The study assumes the Earth habitability is jeopardized if the magnetopause collapses into the Earth surface, that is to say, the solar wind can precipitates directly towards the Earth.

Low field periods with Earth magnetic field intensities below 10 μT (Proterozoic eon as well as the Cambrian, Denovian, Carboniferous, and the Triassic periods; Heunemann et al. 2004; Elming et al. 2009; Hawkins et al. 2019a, 2021; Thallner et al. 2021) and between 10 and 20 μT (Paleo-Archean and Meso-Archean eras, Proterozoic eon, Jurassic, and Paleogene periods in the Cenozoic era; Prevot et al. 1990; Kosterov et al. 1997; Morimoto et al. 1997; Juarez et al. 1998; Di Chiara et al. 2017; Calvo-Rathert et al. 2021) are analysed using dipolar field models with 5 and 15 μT . High field (Hadean eon and the Eo-Archean era; Hale & Dunlop 1984; Tarduno et al. 2020) and standard field periods (Meso-Proterozoic and Neo-Archean eras as well as the Neogene and Quaternary periods; Yoshihara & Hamano 2000; Di Chiara et al. 2021; Kaya et al. 2023) are reproduced by dipolar models with 45 and 30 μT , respectively. In addition, weak multipolar fields linked to geomagnetic reversals (Proterozoic age as well as the Devonian and Cretaceous periods; Guyodo & Valet 1999; Lhuillier et al. 2016; Shcherbakova et al. 2017) are analysed using Earth magnetic field models with quadrupole–dipole coefficient ratios of 0.2 and 0.5 and field intensities of 5 and 15 μT . The Earth magnetic field decay in the Postterum eons is studied

Table 6. Earth habitability along the Sun's evolution on the main sequence during ICME-like space weather conditions comparing the critical B_{IMF} calculated for different Earth magnetic field configurations with respect to the IMF intensity. A red cross (blue circle) indicates the space weather conditions may hamper (do not hamper) the Earth habitability.

Eon/Era	Time (My)	45 (μT)	30 (μT)	15 (μT)	(15, 0.2) ($\mu\text{T}, Q/D$)	(15, 0.5) ($\mu\text{T}, Q/D$)	5 (μT)	(5, 0.2) ($\mu\text{T}, Q/D$)	(5, 0.5) ($\mu\text{T}, Q/D$)
Hadean	4400	X	X	X	X	X	X	X	X
Eo-Archean	3850	O	O	X	X	X	X	X	X
Paleo-Archean	3600	O	O	X	X	X	X	X	X
Meso-Archean	3200	O	O	O	X	X	X	X	X
Paleo-Proterozoic	1850	O	O	O	X	X	X	X	X
Meso-Proterozoic	1300	O	O	O	O	O	O	X	X
Neo-Proterozoic	825	O	O	O	O	O	O	X	X
Paleozoic	350	O	O	O	O	O	O	X	X
Posteriorum	+1500	O	O	O	O	O	O	O	X
Posteriorum	+3000	O	O	O	O	O	O	O	X

using dipolar models with 1 and 0.1 μT , assuming the decline of the geo-dynamo.

The simulations results indicate a dipole with $\geq 5 \mu\text{T}$ can protect the Earth during quiet space weather conditions for all the geological times, except multipolar models with 5 μT and $Q/D \geq 0.2$ during the Hadean eon (including the young sun activity and cyclic modulation). On the other hand, ICME-like space weather conditions require a dipolar magnetic field of $\geq 30 \mu\text{T}$ to protect the Earth from the Archean eon, although a dipolar field with 15 μT only provides an efficient shielding from the Mesoarchean era and a dipolar field with 5 μT from the Meso-Proterozoic era. It should be noted that the Earth habitability is strongly jeopardized during multipolar low field periods compared to dipole low field periods. Indeed, multipolar field periods with 15 μT and $Q/D = 0.2$ cannot provide an efficient magnetic shielding until the Meso-Proterozoic. In addition, multipolar fields with $\leq 5 \mu\text{T}$ and $Q/D \geq 0.2$ are unable to protect the Earth in the Paleozoic era and Posteriorum eons. Finally, a decaying Earth magnetic field in Posteriorum eons cannot protect the Earth during ICME events if the dipole intensity decreases below 1 μT , or during quiet space weather conditions if the field intensity is $\leq 0.1 \mu\text{T}$. Table 6 summarizes the geological eras with impacted habitability conditions for each Earth magnetic field configuration analyzed during ICME-like space weather states.

The analysis results obtained using different models to predict the space weather conditions during the Sun main sequence are compared, particularly Grießmeier et al. (2007), Vidotto et al. (2014), Carolan et al. (2019), and Ahuir et al. (2020) models. Some deviations are identified although the main conclusions of the analysis are the same.

The study shows that the Earth atmosphere was exposed to the SW erosion during the Hadean eon, enhancing the water molecules escape as well as the fast hydrogen and helium exhaust (Shaw 2008; Kasting 2014; Thomassot et al. 2015). The SW erosion during dipolar low field periods in the Archean eon and Paleo-Proterozoic era may also have an effect on the evolution of the ancient Earth atmosphere. In addition, multipolar low field periods with $\leq 5 \mu\text{T}$ and $Q/D \geq 0.5$ during geomagnetic reversals may lead to an inefficient atmosphere protection in the Phanerozoic eon, identified as a possible driver of climate changes in the Earth by several authors (Fairbridge 1977; Verosub & Banerjee 1977; Schneider, Kent & Mello 1992; Worm 1997; Valet et al. 2014).

The implications of our results regarding the SW sterilizing effect on the Earth surface indicate potential effects on the survival and evolution of mats and bacteria from the Paleo-Archean era

(Lepot 2020) as well as the multicellular organism from the Meso-Proterozoic era (Butterfield 2000). Life in the Phanerozoic eon can be also hampered during geomagnetic reversals, linked in several studies with mass-extinction (Kennett & Watkins 1970; Plotnick 1980; Worm 1997; Isozaki 2009; Wei et al. 2014; Isozaki & Servais 2018).

The analysis of the ionosphere expansion induced by large EUV and X-ray fluxes in the Hadean and Archean eons, particularly the effect on the bow shock and magnetopause standoff distances, indicates a relaxation of the SW constraints on the Earth habitability requirements. The bow shock and magnetopause standoff distances increase as the ionosphere expands showing an averaged increment ratio of 0.52 and 0.46, respectively. The large SW dynamic pressure in the Hadean and Archean eons induces a strong compression of the ionosphere, partially counterbalancing the increment of the bow shock and magnetopause standoff distance as the ionosphere expands. On the other hand, IMF lines pile up in the bow shock region leading to a further extension of the bow shock standoff distance while the magnetopause standoff distance decreases, particularly if the IMF is Southward. Including the ionosphere expansion in the model does not change the analysis results for quiet space weather conditions during the Hadean and Archean eons, because the simulation set performed ignoring this effect already indicates the Earth magnetic field provided an efficient protection. Nevertheless, ICME-like space weather conditions must be studied including the expansion of the ionosphere to improve the analysis accuracy.

We conclude that the hamper of space weather on the Earth habitability must be considered as an important driver of the atmosphere and life evolution. It must be recalled that there are other important external actuators not included in the study such as impacts events as Geo-crossing asteroids or comets, gamma ray burst, supernovas (cosmic rays) as well as the ultraviolet and X rays radiation generated by the Sun. Impacting events produce dust and aerosols that can cover the Earth atmosphere during tens to hundred of years inhibiting photosynthesis (Alvarez et al. 1984). An impacting event was the most probable driver of the Cretaceous–Paleogene extinction event (Schulte et al. 2010). Gamma ray burst may cause the destruction of the Earth's ozone layer that brings protection against the ultraviolet radiation and could be responsible of the late Ordovician mass extinction (Melott et al. 2004; Thomas et al. 2005). Supernova radiation produces strong ionization effects and induce mass extinction events too (Whitmire & Jackson 1984; Ellis & Schramm 1995; Dar, Laor & Shaviv 1998; Svensmark 2012). Likewise, ultraviolet and X rays radiation from the Sun, particularly at the early phases of the Sun evolution, may have

an harmful effect on biological structures and could play a role in life evolution (Cockell 2000; Dartnell 2011; Lammer et al. 2011; Airapetian et al. 2017; Kaltenecker 2017). On top of that, high X-ray and EUV fluxes generated by the young Sun will also be responsible for high neutral loss rates of the atmosphere (Tian et al. 2008a, b; Johnstone et al. 2021a). Nevertheless, the atmospheric erosion and surface sterilization caused by the SW should be included in the list of the most important external effects in considering solar-type Earth and exoplanets habitability along the Sun and other stars evolution.

ACKNOWLEDGEMENTS

This work was supported by the project 2019-T1/AMB-13648 founded by the Comunidad de Madrid. The research leading to these results has received funding from the grants ERC WholeSun 810218, Exoplanets A, INSU/PNP. PZ acknowledges funding from the ERC No 101020459 – Exoradio. We extend our thanks to CNES for Solar Orbiter, PLATO and Meteo Space science support and to INSU/PNST for their financial support. This work has been supported by Comunidad de Madrid (Spain) – multiannual agreement with UC3M (‘Excelencia para el Profesorado Universitario’ - EPUC3M14) – Fifth regional research plan 2016–2020. Data available on request from the authors.

DATA AVAILABILITY

4.3 version of the PLUTO code used for performing the simulations is available via <http://plutocode.ph.unito.it> and developed openly at the Dipartimento di Fisica, Torino University in a joint collaboration with INAF, Osservatorio Astronomico di Torino and the SCAI Department of CINECA (Mignone et al., 2007).

REFERENCES

- Ahuir J., Brun A. S., Strugarek A., 2020, *A&A*, 635, A170
- Airapetian V. S., 2016, Proc. IAU Symp. 12, Living Around Active Stars. Kluwer, Dordrecht, p. 315
- Airapetian V. S., Gloer A., Danchi W., 2014
- Airapetian V. S. et al., 2020, *Int. J. Astrobiol.*, 19, 136
- Airapetian V., Gloer A., Guillaume G., 2015, Proc. IAU Symp. 11, Solar and Stellar Flares and their Effects on Planets. Kluwer, Dordrecht, p. 409
- Airapetian V. S., Gloer A., Khazanov G. V., Loyd R. O. P., France K., Sojka J., Danchi W. C., Liemohn M. W., 2017, *ApJ*, 836, L3
- Alvarez W., Kauffman E. G., Surlyk F., Alvarez L. W., Asaro F., Michel H. V., 1984, *Science*, 223, 1135
- Andréevová K., Pulkkinen T. I., Laitinen T. V., Přeč L., 2008, *J. Geophys. Res.: Space Phys.*, 113, A09224
- Aubert J., Labrosse S., Poutou C., 2009, *Geophys. J. Int.*, 179, 1414
- Aubert J., Tarduno J. A., Johnson C. L., 2010, *Space Sci. Rev.*, 155, 337
- Aubert J., Livermore P. W., Finlay C. C., Fournier A., Gillet N., 2022, *Geophys. J. Int.*, 231, 650
- Balona L. A., 2012, *MNRAS*, 423, 3420
- Barnes S. A., 2003, *ApJ*, 586, 464
- Benton M. J., Twitchett R. J., 2003, *Trends Ecol. Evol.*, 18, 358
- Blackman E. G., Tarduno J. A., 2018, *MNRAS*, 481, 5146
- Bogue S. W., Merrill R. T., 1992, *Annu. Rev. Earth Planet. Sci.*, 20, 181
- Buccino A. P., Lemarchand G. A., Mauas P. J. D., 2007, *Icarus*, 192, 582
- Butterfield N. J., 2000, *Paleobiology*, 26, 386
- Büchner J., Dum C., Scholer M., 2003, *Space Plasma Simulation*. Springer-Verlag, Berlin, Heidelberg
- Cairns I. H., Lyon J. G., 1995, *J. Geophys. Res.: Space Phys.*, 100, 17173
- Cairns I. H., Lyon J. G., 1996, *Geophys. Res. Lett.*, 23, 2883
- Calvo-Rathert M., Bogalo M. F., Morales J., Goguitchaichvili A., Lebedev V. A., Vashakidze G., Garcia-Redondo N., Herrero-Bervera E., 2021, *J. Geophys. Res.: Solid Earth*, 126, e2020JB020019
- Cane H. V., Richardson I. G., 2003, *J. Geophys. Res.: Space Phys.*, 108, 1
- Cane H. V., Richardson I. G., St. Cyr O. C., 2000, *Geophys. Res. Lett.*, 27, 3591
- Cannon P. et al., 2013, Technical Report, Extreme Space Weather: Impacts On Engineered Systems And Infrastructure, Royal Academy of Engineering, London
- Carolan S., Vidotto A., Loesch C., Coogan P., 2019, *MNRAS*, 489, 5784
- Carrington R. C., 1859, *MNRAS*, 20, 13
- Catling D. C., Zahnle K. J., 2020, *Sci. Adv.*, 6, eaax1420
- Chebly J. J., Alvarado-Gómez J. D., Poppenhaeger K., 2022, *Astron. Nachr.*, 343, e210093
- Choi H.-S. et al., 2011, *Space Weather*, 9, S06001
- Cockell C. S., 2000, *Orig. Life Evol. Biosph.*, 30, 467
- Dar A., Laor A., Shaviv N. J., 1998, *Phys. Rev. Lett.*, 80, 5813
- Dartnell L., 2011, *Astron. Geophys.*, 52, 25
- Davies C. J., Bono R. K., Meduri D. G., Aubert J., Greenwood S., Biggin A. J., 2021, *Geophys. J. Int.*, 228, 316
- Den M. et al., 2006, *Space Weather*, 4, S06004
- Di Chiara A., Muxworthy A. R., Trindade R. I. F., Bispo-Santos F., 2017, *Geochem. Geophys. Geosyst.*, 18, 3891
- Di Chiara A. et al., 2021, *Geochem. Geophys. Geosyst.*, 22, e2020GC009605
- Dodd M. S., Papineau D., Grenne T., Slack J. F., Rittner M., Pirajno F., O’Neil J., Little C. T. S., 2017, *Nature*, 543, 60
- Driscoll P. E., 2016, *Geophys. Res. Lett.*, 43, 5680
- Dubin E. et al., 2019, *J. Geophys. Res.: Space Phys.*, 124, 9725
- Dušák Š., Granko G., Šafránková J., Němeček Z., Jelínek K., 2010, *Geophys. Res. Lett.*, 37, L19103
- Ellis J., Schramm D. N., 1995, *Proc. Natl. Acad. Sci.*, 92, 235
- Elming S. A., Moakhar M. O., Layer P., Donadini F., 2009, *Geophys. J. Int.*, 179, 59
- Emeriau-Viard C., Brun S., 2017, *ApJ*, 846, 26
- Fabbian D. et al., 2017, *Astron. Nachr.*, 338, 753
- Facsó G. et al., 2016, *Space Weather*, 14, 351
- Fairbridge R. W., 1977, *Nature*, 265, 430
- Finlay C. C. et al., 2010, *Geophys. J. Int.*, 183, 1216
- Folsom C. P. et al., 2017, *MNRAS*, 474, 4956
- Gallet F., Bouvier J., 2015, *A&A*, 577, A98
- Gallet F., Charbonnel C., Amard L., Brun S., Palacios A., Mathis S., 2017, *A&A*, 597, A14
- Garraffo C., Drake J. J., Cohen O., 2016, *ApJ*, 833, L4
- Glatzmaiers G. A., Roberts P. H., 1995, *Nature*, 377, 203
- Gombosi T. I., 1994, *Gaskinetic Theory*, Cambridge Atmospheric and Space Science Series, Cambridge Univ. Press, Cambridge
- González Hernández I., Komm R., Pevtsov A., Leibacher J., 2014, *Solar Origins of Space Weather and Space Climate*. Springer-Verlag, New York
- Gosling J. T., 1990, *Coronal Mass Ejections and Magnetic Flux Ropes in Interplanetary Space*. American Geophysical Union (AGU), Washington, DC, p. 343
- Gosling J. T., McComas D. J., Phillips J. L., Bame S. J., 1991, *J. Geophys. Res.: Space Phys.*, 96, 7831
- Grießmeier J.-M., Zarka P., Spreew H., 2007, *A&A*, 475, 359
- Grygorov K., Šafránková J., Němeček Z., Pi G., Přeč L., Urbář J., 2017, *Planet. Space Sci.*, 148, 28
- Gubbins G., 2008, *Science*, 452, 165
- Guinan E. F., Ribas I., 2002, in Montesinos B., Gimenez A., Guinan E. F., eds, ASP Conf. Ser. Vol. 269, The Evolving Sun and its Influence on Planetary Environments. Astron. Soc. Pac., San Francisco, p. 85
- Guyodo Y., Valet J., 1999, *Nature*, 399, 249
- Hale C. J., Dunlop D. J., 1984, *Geophys. Res. Lett.*, 11, 97
- Han Q. et al., 2020, *Earth Planet. Phys.*, 4, 73
- Hapgood M., 2019, *Space Weather*, 17, 950
- Hawkins L. M. A., Anwar T., Shcherbakova V., Biggin A., Kravchinsky V., Shatsillo A., Pavlov V., 2019a, *Earth Planet. Sci. Lett.*, 506, 134
- Hawkins L. M. A., Anwar T., Shcherbakova V. V., Biggin A. J., Kravchinsky V. A., Shatsillo A., Pavlov V., 2019b, *Earth Planet. Sci. Lett.*, 506, 134

- Hawkins L. M. A., Grappone J. M., Sprain C. J., Saengduan P., Sage E. J., Cunningham S. T., Kugabalan B., Biggin A. J., 2021, *Proc. Natl. Acad. Sci.*, 118, e2017342118
- Heunemann C., Krása D., Soffel H. C., Gurevitch E., Bachtadse V., 2004, *Earth Planet. Sci. Lett.*, 218, 197
- Honkonen I., Rastätter L., Grocott A., Pulkkinen A., Palmroth M., Raeder J., Ridley A. J., Wiltberger M., 2013, *Space Weather*, 11, 313
- Howard R. A., 2006, A Historical Perspective on Coronal Mass Ejections. American Geophysical Union (AGU), Washington, DC, p. 7
- Howard T., 2014, *Space Weather and Coronal Mass Ejections*. Springer-Verlag, New York
- Huttunen K. E. J., Koskinen H. E. J., Pulkkinen T. I., Pulkkinen A., Palmroth M., Reeves E. G. D., Singer H. J., 2002, *J. Geophys. Res.: Space Phys.*, 107, SMP 15
- Isozaki Y., 2009, *Gondwana Res.*, 15, 421
- Isozaki Y., Servais T., 2018, *Lethaia*, 51, 173
- Jakosky B. M., Grebowsky J. M., Luhmann J. G., Brain D. A., 2015, *Geophys. Res. Lett.*, 42, 8791
- Jardine M., Collier A. C., 2018, *MNRAS*, 482, 2853
- Jia X., Slavín J. A., Gombosi T. I., Daldorff L. K. S., Toth G., Holst B., 2015, *J. Geophys. Res. (Space Phys.)*, 120, 4763
- Johnstone C. P., Güdel M., Brött I., Lüftinger T., 2015, *A&A*, 577, A28
- Johnstone C. P., Lammer H., Kislyakova K. G., Scherf M., Güdel M., 2021a, *Earth Planet. Sci. Lett.*, 576, 117197
- Johnstone C. P., Bartel M., Güdel M., 2021b, *A&A*, 649, A96
- Jones C. A., 2011, *Annu. Rev. Fluid Mech.*, 43, 583
- Juarez M. T., Tauxe L., Gee J. S., Pick T., 1998, *Nature*, 394, 878
- Kabin K., Gombosi T. I., DeZeeuw D. L., Powell K. G., 2000, *Icarus*, 143, 397
- Kabin K. et al., 2008, *Icarus*, 195, 1
- Kaltenegger L., 2017, *ARA&A*, 55, 433
- Kasting J. F., 1993, *Science*, 259, 920
- Kasting J. F., 2014, *Earth's Early Atmosphere and Surface Environment*. Geological Society of America, Boulder, CO
- Kay C., Gopalswamy N., Reinard A., Opher M., 2017, *ApJ*, 835, 117
- Kaya N., Hisarlı Z. M., Nowaczyk N. R., Makaroglu O., 2023, *Geophys. J. Int.*, 233, 1708
- Kennett J., Watkins N., 1970, *Nature*, 227, 930
- Khodachenko M. L. et al., 2007, *Astrobiology*, 7, 167
- Kilpua E. K. J., Lugaz N., Mays M. L., Temmer M., 2019, *Space Weather*, 17, 498
- Kislyakova K. G., Johnstone C. P., Scherf M., Holmstrom M., Alexeev I. I., Lammer H., Khodachenko M. L., Güdel M., 2020, *J. Geophys. Res.: Space Phys.*, 125, e2020JA027837
- Kosterov A. A., Prevot M., Perrin M., Shashkanov V. A., 1997, *J. Geophys. Res.: Solid Earth*, 102, 24859
- Laitinen T. V., Pulkkinen T. I., Palmroth M., Janhunen P., Koskinen H. E. J., 2005, *Ann. Geophys.*, 23, 3753
- Lammer H. et al., 2007, *Astrobiology*, 7, 85
- Lammer H. et al., 2011, *Orig. Life Evol. Biosph.*, 41, 503
- Lammer H. et al., 2018, *A&AR*, 26, 1
- Lembege B., Cai D. S., Ekawati S., 2022, *ApJ*, 937, 127
- Lepot K., 2020, *Earth Sci. Res.*, 209, 103296
- Lhuillier F. et al., 2016, *Geophys. Res. Lett.*, 43, 6170
- Lichtenegger H. I. M., Lammer H., Griebmeier J. M., Kulikov Y. N., von Paris P., Hausleitner W., Krauss S., Rauer H., 2010, *Icarus*, 210, 1
- Linsky J., 2019, *Space Weather: The Effects of Host Star Flares on Exoplanets*. Springer International Publishing, Heidelberg, Germany, p. 229
- Liu Z.-Q. et al., 2015, *J. Geophys. Res.: Space Phys.*, 120, 5645
- Low B. C., 2001, *J. Geophys. Res.: Space Phys.*, 106, 25141
- Lugaz N., 2019, *Space Weather at Earth and in Our Solar System, The Sun as a Guide to Stellar Physics*, Elsevier, p.335
- Lugaz N., Farrugia C. J., Huang C.-L., Spence H. E., 2015, *Geophys. Res. Lett.*, 42, 4694
- Lundin R., Lammer H., Ribas I., 2007, *Space Sci. Rev.*, 129, 245
- Maehara H. et al., 2012, *Nature*, 485, 478
- Maehara H., Shibayama T., Notsu S., Notsu Y., Honda S., Nogami D., Shibata K., 2015, *Earth Planets Space*, 67, 59
- Manchester W. B. IV, Gombosi T. I., Roussev I., Ridley A., De Zeeuw D. L., Sokolov I. V., Powell K. G., Tóth G., 2004, *J. Geophys. Res.: Space Phys.*, 109, A02107
- Mays M. L. et al., 2015, *Sol. Phys.*, 290, 1775
- McElhinny M. W., 1971, *Science*, 172, 157
- McElhinny M. W., McFadden P. L., 1998, *The Magnetic Field of the Earth: Paleomagnetism, the Core, and the Deep Mantle*. Vol. 63. Academic Press, London
- McGhee G. R., 1988, *Paleobiology*, 14, 250
- Mejnertsen L., Eastwood J. P., Hietala H., Schwartz S. J., Chittenden J. P., 2018, *J. Geophys. Res.: Space Phys.*, 123, 259
- Melott A. L. et al., 2004, *Int. J. Astrobiol.*, 3, 55
- Mignone A., Bodo G., Massaglia S., Matsakos T., Tesileanu O., Zanni C., Ferrari A., 2007, *ApJS*, 170, 228
- Molera Calvés G. et al., 2014, *A&A*, 564, A4
- Moore T. E., Khazanov G. V., 2010, *J. Geophys. Res.: Space Phys.*, 115, A00J13
- Morimoto C., Otofujii Y., Miki M., Tanaka H., Itaya T., 1997, *Geophys. J. Int.*, 128, 585
- Morse J. W., Mackenzie F. T., 1998, *Aquat. Geochem.*, 4, 301
- Neugebauer M., Goldstein R., 1997, *Washington DC American Geophysical Union Geophysical Monograph Series*, Vol. 99, Washington, DC, p. 245
- Newkirk G., Jr, 1980, *The Ancient Sun: Fossil Record in the Earth, Moon and Meteorites*, Pergamon Press, New York
- Ngwira C. M. et al., 2013, *Space Weather*, 11, 671
- Nwankwo V. U. J., Chakrabarti S. K., Weigel R. S., 2015, *Adv. Space Res.*, 56, 47
- Němeček Z., Šafránková J., Koval A., Merka J., Přech L., 2011, *J. Atmos. Sol. Terr. Phys.*, 73, 20
- Němeček Z., Šafránková J., Lopez R. E., Dušek Š., Nouzák L., Přech L., Šimůnek J., Shue J.-H., 2016, *Adv. Space Res.*, 58, 240
- Ogino T., Walker R. J., Ashour-Abdalla M., 1992, *IEEE T. Plasma Sci.*, 20, 817
- Omelchenko Y. A., Roytershteyn V., Chen L. J., Ng J., Hietala H., 2021, *J. Atmos. Sol. Terr. Phys.*, 215, 105581
- Onoue T., Takahata N., Miura M., Sato H., Ishikawa A., Soda K., Sano Y., Isozaki Y., 2019, *Prog. Earth Planet. Sci.*, 6, 1
- Parnell J., Boyce A. J., Mark D., Bowden S., Spinks S., 2010, *Nature*, 468, 290
- Paul A., Vaidya B., Strugarek A., 2022, *ApJ*, 938, 130
- Pizzolato N., Maggio A., Micela G., Sciortino S., Ventura P., 2003, *A&A*, 397, 147
- Plotnick R. E., 1980, *Geology*, 8, 578
- Poppe B. B., Jordan K. P., 2006, *Sentinels of the Sun: Forecasting Space Weather*. Johnson Books, Denver, CO
- Poreda R. J., Becker L., 2003, *Astrobiology*, 3, 75
- Prevot M., Derder M. E., McWilliams M., Thompson J., 1990, *Earth Planet. Sci. Lett.*, 97, 129
- Raeder J. et al., 2001, *J. Geophys. Res.: Space Phys.*, 106, 381
- Regnault F., Janvier M., Demoulin P., Auchere F., Strugarek A., Dasso S., Nous C., 2020, *J. Geophys. Res.: Space Phys.*, 125, e2020JA028150
- Regnault F., Al-Haddad N., Lugaz N., Farrugia C., Yu W., 2022, 44th COSPAR Scientific Assembly. Held 16–24 July Athens, Greece, p. 2438
- Reiners A., Schussler M., Passegger V. M., 2014, *ApJ*, 794, 144
- Ribas I., Guinan E., Güdel M., Audard M., 2005, *ApJ*, 622, 680
- Richardson I. G., Cliver E. W., Cane H. V., 2001, *Geophys. Res. Lett.*, 28, 2569
- Riley P., 2012, *Space Weather*, 10, S02012
- Roberts P. H., Glatzmaier G. A., 2001, *Geophys. Astrophys. Fluid Dyn.*, 94, 47
- Roberts J. H., Lillis R. J., Manga M., 2009, *J. Geophys. Res.: Planets*, 114, E04009
- Rodgers-Lee D., Taylor A. M., Vidotto A. A., Downes T. P., 2021, *MNRAS*, 504, 1519
- Rodriguez-Mozos J. M., Moya A., 2019, *A&A*, 630, A52
- Réville V., Folsom C. P., Strugarek A., Brun A. S., 2016, *ApJ*, 832, 145
- Salman T. M., Lugaz N., Farrugia C. J., Winslow R. M., Galvin A. B., Schwadron N. A., 2018, *Space Weather*, 16, 2004

- Samsonov A. A., Sibeck D. G., Imber J., 2007, *J. Geophys. Res.: Space Phys.*, 112, A12220
- Samsonov A. A., Bogdanova Y. V., Branduardi-Raymont G., Sibeck D. G., Toth G., 2020, *Geophys. Res. Lett.*, 47, e2019GL086474
- Sanz-Forcada J., Ribas I., Micela G., Pollock A. M. T., Garcia-Alvarez D., Solano E., Eiroa C., 2010, *A&A*, 511, L8
- Savani N. P. et al., 2017, *Space Weather*, 15, 441
- Schaefer B. E., King J. R., Deliyannis C. P., 2000, *ApJ*, 529, 1026
- Schneider D. A., Kent D. V., Mello G. A., 1992, *Earth Planet. Sci. Lett.*, 111, 395
- Schoepfer S. D., Algeo T. J., van de Schootbrugge B., Whiteside J. H., 2022, *Earth Sci. Rev.*, 232, 104099
- Schulte P. et al., 2010, *Science*, 327, 1214
- Schwarz E., Symons D. T. A., 1969, *Phys. Earth Planet. Inter.*, 2, 11
- Schwenn R., Dal Lago A., Huttunen E., Gonzalez W. D., 2005, *Ann. Geophys.*, 23, 1033
- Scolini C., Verbeke C., Poedts S., Chané E., Pomoell J., Zuccarello F. P., 2018, *Space Weather*, 16, 754
- See V., Jardine M., Vidotto A. A., Petit P., Marsden S. C., Jeffers S. V., do Nascimento J. D., 2014, *A&A*, 570, A99
- See V. et al., 2017, *MNRAS*, 466, 1542
- Shaw G. H., 2008, *Geochemistry*, 68, 235
- Shaw J. A., 2019, in Creath K., Lakshminarayanan V., Shaw J. A., eds, Proc. SPIE Conf. Ser. Vol. 11099, Light in Nature VII. SPIE, Bellingham, p. 28
- Shcherbakova V. V., Biggin A. J., Veselovskiy R. V., Shatsillo A. V., Hawkins L. M. A., Shcherbakov V. P., Zhidkov G. V., 2017, *Geophys. J. Int.*, 209, 1265
- Sheeley N. R., Jr, Howard R. A., Koomen M. J., Michels D. J., Schwenn R., Mühlhäuser K. H., Rosenbauer H., 1985, *J. Geophys. Res.: Space Phys.*, 90, 163
- Shen F., Feng X. S., Wu S. T., Xiang C. Q., Song W. B., 2011, *J. Geophys. Res.: Space Phys.*, 116, A04102
- Shibayama T. et al., 2013, *ApJS*, 209, 5
- Sibeck D. G., Lopez R. E., Roelof E. C., 1991, *J. Geophys. Res.: Space Phys.*, 96, 5489
- Sihver L., Mortazavi S. M. J., 2021, *J. Biomed. Phys. Eng.*, 1, 663
- Skumanich A., 1972, *ApJ*, 171, 565
- Skumanich A., 2019, *ApJ*, 878, 35
- Slavin J. A., Holzer R. E., 1979, *J. Geophys. Res.*, 84, 2076
- Slavin J. A. et al., 2009, *Science*, 324, 606
- Smirnov A. V., Kulakov E. V., Foucher M. S., Bristol K. E., 2017, *Sci. Adv.*, 3, e1602306
- Sterenberg M. G., Cohen O., Drake J. J., Gombosi T. I., 2011, *J. Geophys. Res.: Space Phys.*, 116, A01217
- Strugarek A., Brun A. S., Matt S. P., Réville V., 2014, *ApJ*, 795, 86
- Strugarek A., Brun A. S., Matt S. P., Réville V., 2015, *ApJ*, 815, 111
- Svensmark H., 2012, *MNRAS*, 423, 1234
- Tarduno J. A., Cottrell R. D., Watkeys M. K., Bauch D., 2007, *Nature*, 446, 657
- Tarduno J. A. et al., 2010, *Science*, 327, 1238
- Tarduno J. A., Blackman E. G., Mamajek E. E., 2014, *Phys. Earth Planet. Inter.*, 233, 68
- Tarduno J. A. et al., 2020, *Proc. Natl. Acad. Sci.*, 117, 2309
- Thallner D., Biggin A. J., McCausland P. J. A., Fu R. R., 2021, *J. Geophys. Res.: Solid Earth*, 126, e2021JB022292
- Thomas B. C. et al., 2005, *ApJ*, 634, 509
- Thomassot E., O’Neil J., Francis D., Cartigny P., Wing B. A., 2015, *Proc. Natl. Acad. Sci.*, 112, 707
- Tian F., Kasting J. F., Liu H.-L., Roble R. G., 2008a, *J. Geophys. Res.: Planets*, 113, 1
- Tian F., Solomon S. C., Qian L., Lei J., Roble R. G., 2008b, *J. Geophys. Res.: Planets*, 113, 1
- Torok T. et al., 2018, 856, 75
- Toth G., 1996, *Astrophys. Lett. Commun.*, 34, 245
- Tu L., Johnstone C. P., Gudel M., Lammer H., 2015, *AA*, 577, L3
- Valet J. P., Fournier A., 2016, *Rev. Geophys.*, 54, 410
- Valet J. P., Fournier A., Courtillot V., Herrero-Bervera E., 2012, *Nature*, 490, 89
- Valet J.-P. et al., 2014, *Earth Planet. Sci. Lett.*, 397, 67
- van der Boon A. et al., 2022, *Earth Sci. Rev.*, 231, 104073
- van Zijl J. S. V., Graham K. W. T., Hales A. L., 1962, *Geophys. J. R. Astron. Soc.*, 7, 169
- Varela J., Pantellini F., Moncuquet M., 2015, *Planet. Space Sci.*, 119, 264
- Varela J., Pantellini F., Moncuquet M., 2016a, *Planet. Space Sci.*, 120, 78
- Varela J., Pantellini F., Moncuquet M., 2016b, *Planet. Space Sci.*, 122, 46
- Varela J., Pantellini F., Moncuquet M., 2016c, *Planet. Space Sci.*, 125, 80
- Varela J., Pantellini F., Moncuquet M., 2016d, *Planet. Space Sci.*, 129, 74
- Varela J., Reville V., Brun A. S., Pantellini F., Zarka P., 2016e, *A&A*, 595, A69
- Varela J., Reville V., Brun A. S., Zarka P., Pantellini F., 2018, *A&A*, 616, A182
- Varela J., Brun A. S., Zarka P., Strugarek A., Pantellini F., Reville V., 2022a, *Space Weather*, 20, e2022SW003164
- Varela J., Reville V., Brun A. S., Zarka P., Pantellini F., 2022b, *A&A*, 659, A10
- Verosub K. L., Banerjee S. K., 1977, *Rev. Geophys.*, 15, 145
- Vidotto A. A. et al., 2014, *MNRAS*, 441, 2361
- Wang J. Y., Wang C., Huang Z. H., Sun T. R., 2014, *J. Geophys. Res.: Space Phys.*, 119, 1887
- Wang M., Lu J., Liu Z., Pei S., 2012, *Chin. Sci. Bull.*, 57, 1438
- Wang Y. L., Raeder J., Russell C. T., Phan T. D., Manapat M., 2003, *J. Geophys. Res.: Space Phys.*, 108, SMP 8
- Wang Y. L., Raeder J., Russell C. T., 2004, *Ann. Geophys.*, 22, 1001
- Wang Y. M., Ye P. Z., Wang S., Xue X. H., 2003, *Geophys. Res. Lett.*, 30, 1
- Weber E. J., Davis L. J., 1967, *ApJ*, 148, 217
- Wei Y. et al., 2014, *Earth Planet. Sci. Lett.*, 394, 94
- Whitmire D. P., Jackson A. A. IV, 1984, *Nature*, 308, 713
- Wood B. E., Muller H. R., Zank G. P., Linsky J. L., Redfield S., 2005, *ApJ*, 628, L143
- Worm H.-U., 1997, *Earth Planet. Sci. Lett.*, 147, 55
- Wu C., Lepping R. P., 2015, *Sol. Phys.*, 290, 1243
- Wu C.-C., Lepping R. P., 2002, *J. Geophys. Res.: Space Phys.*, 107, SSH 3
- Wu C.-C., Lepping R. P., Gopalswamy N., 2006, *Sol. Phys.*, 239, 449
- Wu C.-C. et al., 2016, *J. Geophys. Res.: Space Phys.*, 121, 1839
- Xu X. et al., 2015, *Sci. Rep.*, 5, 8080
- Yoshihara A., Hamano Y., 2000, *Phys. Earth Planet. Inter.*, 117, 295
- Zenchenko T. A., Breus T. K., 2021, *Atmosphere*, 12, 1
- Zendejas J., Segura A., Raga A., 2010, *Icarus*, 210, 539
- Zhang H. et al., 2022, *ApJ*, 937, 1

APPENDIX A: EXTENDED IONOSPHERE MODEL

The ionosphere model is upgraded to evaluate the effect of the ionosphere expansion on the bow shock and magnetopause standoff distance. The ionospheric domain is now divided in two sections. At $R = 2.3 - 2.5R_E$, it is defined the coupling region between the upper atmosphere and the ionosphere. From $R = 2.5R_E$ to the ionosphere upper limit (an input of the model) is defined the upper ionosphere region.

Special conditions are imposed in the coupling region between the upper atmosphere and the ionosphere. The plasma density is stratified with respect to the Alfvén velocity and the module of the Alfvén velocity is fixed ($v_A = 2 \times 10^4 \text{ km s}^{-1}$) and does not evolve

during the simulation, defined as

$$\rho = \frac{|B|^2}{\mu_0 v_A^2}. \quad (\text{A1})$$

The hydro-static equilibrium between the upper atmosphere and the ionosphere is set by fixing the plasma pressure with respect to the sound speed of the SW (c_{sw}) and the upper atmosphere (c_p):

$$p = \frac{n}{\gamma} \left(\frac{(c_p - c_{sw})(r^3 - R_s^3)}{R_{un}^3 - R_s^3} + c_{sw} \right)^2, \quad (\text{A2})$$

with $c_p = \sqrt{\gamma K_B T_p / m_p}$ with T_p the plasma temperature at the upper atmosphere and T_{sw} the SW temperature.

The plasma density and magnetic field are free to evolve in the upper ionosphere region, thus the upper ionosphere can be compressed by the effect of the SW as well as the Earth magnetic field lines. Only the slope of the pressure is constrained following equation (A2).

The field-aligned currents (J_{FAC}) are calculated in the upper ionosphere and the coupling region between the upper atmosphere and the ionosphere based on (Büchner et al. 2003) model:

$$\mathbf{J}_{FAC} = \mathbf{J} - \mathbf{J}_\perp, \quad (\text{A3})$$

where

$$\mathbf{J} = \frac{1}{\mu_0} \nabla \times \mathbf{B}, \quad (\text{A4})$$

$$\mathbf{J}_\perp = \mathbf{J} - \frac{J_r B_r + J_\theta B_\theta + J_\phi B_\phi}{|B|^2} \mathbf{B}, \quad (\text{A5})$$

with \mathbf{J} the plasma current, \mathbf{J}_\perp the perpendicular component of the plasma current along the magnetic field line, μ_0 the vacuum magnetic permeability, and \mathbf{B} the magnetic field.

Next, the electric field is calculated using the Pedersen conductance (σ) empirical formula,

$$\sigma = \frac{40 E_0 \sqrt{F_E}}{16 + E_0^2}, \quad (\text{A6})$$

with $E_0 = K_B T_E$ the mean energy of the electrons, $F_E = n_E \sqrt{E_0 / (2\pi m_E)}$ the energy flux, and K_B the Boltzmann constant (T_E and m_E are the electron temperature and mass, respectively). Thus, the electric field (E) linked to the FAC is:

$$\mathbf{E} = \sigma \mathbf{J}_{FAC}. \quad (\text{A7})$$

When the electric field is calculated, the velocity of the plasma in the coupling region between the upper atmosphere and the ionosphere is:

$$\mathbf{v} = \frac{\mathbf{E} \times \mathbf{B}}{|B|^2}. \quad (\text{A8})$$

This paper has been typeset from a $\text{T}_E\text{X}/\text{L}_A\text{T}_E\text{X}$ file prepared by the author.